POLITECNICO DI MILANO
Scuola di Ingegneria Industriale e dell'Informazione
Corso di Laurea Magistrale in Ingegneria Fisica

Operando SXRD study of Ag(111) oxidation

Relatore: Prof. Giacomo Claudio GHIRINGHELLI

Correlatore: Maciej JANKOWSKI

Tesi Magistrale di:

Anastasia LEONE

Matr. Nr. 823802

Sessione Laurea Dicembre 2016

Anno Accademico 2015-2016

Ringraziamenti

Ringrazio la mia famiglia per tutto il supporto, in particolare mia madre, senza la quale non ce l'avrei mai fatta.

Ringrazio Ale, coinquilino, compagno di studi e soprattutto amico, per i consigli, l'aiuto e il supporto.

Ringrazio tutto lo staff della beamline per la bella esperienza.

Ringrazio tutte le persone che mi sono state vicine in questi anni di università, Luca, Patti e Stefano, grazie per il sostegno e i consigli.

Infine ringrazio Ludovica e Cinzia, per avermi lasciato un bellissimo ricordo del periodo universitario.

Contents

List of Figures

Abstract

The current study was done at the European Synchrotron Radiation Facility (ESRF) in the ID03 Surface Diffraction beamline, under the supervision of Dr. Maciej Jankowski. The topic of this research is the characterisation of the catalytic surface Ag(111). Silver is an important catalyst used for the selective oxidation of ethylene to ethylene oxide, a chemical whose derivatives are largely produced in industry. An optimization of this catalysis would have an huge impact from the economic point of view. For this purpose, the reactive surface species must be identified. Several studies have been done on this topic, but until now this active species is unknown. The past studies have been limited by the condition of Ultra High Vacuum, necessary in surface science, that creates the so-called *pressure gap* between the experiment and the true working conditions of the catalyst. The aim of my work, was to fill this gap by using the Surface X-Ray Diffraction technique to investigate the oxidation of the Ag(111)surface. Before the experiment, the sample was prepared by following typical cleaning surface procedures, such as sputtering and annealing. Then, the cleanliness and the crystallographic quality of the surface, have been checked by AES and LEED measurements. During the experiment we observed two oxygen-induced reconstructions: the well-known p-(4×4) and the bulk oxide. Our hypothesis, based on the observed evidences, is that the synchrotron radiation induces the oxidation process.

Sommario

Questa tesi è il risultato di uno stage svolto a Grenoble, presso ESRF (European Synchrotron Radiation Facility), nella beamline ID03, dedicata allo studio delle superfici, sotto la supervisione del dr. Maciej Jankowski.
L'obiettivo del mio esperimento era quello di caratterizzare la superficie (111) di un cristallo di argento, successivamente alla sua ossidazione. Nanoparticelle di argento vengono utilizzate come catalizzatori, in reazioni di catalisi eterogenea come ad esempio, la reazione di sintesi dell'ossido di etilene. Tale prodotto viene ampiamente utilizzato dall'industria chimica, poiché l'ossido di etilene è un intermedio di reazione nella sintesi del glicol etilenico e dei poliesteri. Si stima che ogni anno vengono prodotti milioni di tonnellate di ossido di etilene, è quindi chiaro, che un'ottimizzazione di tale processo di sintesi comporterebbe un enorme risparmio in termini economici.
La reazione viene catalizzata dalla superficie di argento ossidata, ma il meccanismo di tale processo non è stato ancora completamente caratterizzato. In particolare, non è ancora stata individuata quale tra le possibili ricostruzioni indotte dall'ossidazione sulla superficie del metallo è la fase attiva. Gli esperimenti effettuati in passato si basano sull'utilizzo di tecniche sperimentali che necessitano condizioni di ultra alto vuoto, come la tecnica *Low Energy Electron Diffraction*, la *Scanning Tunneling Microscopy* e infine la *Temperature Desorption Spectroscopy*. Ma, la necessaria condizione di ultra alto vuoto limita i risultati ottenuti dai precedenti studi, in quanto non vengono, durante l'esperimento, simulate le reali condizioni di lavoro di questo catalizzatore, che sono alte temperature e alte pressioni. Infatti, le strutture che durante la catalisi sono energeticamente favorevoli, potrebbero non formarsi a basse pressioni e basse temperature. Il sistema in tale condizioni, potrebbe non essere in grado di fornire l'energia necessaria al superamento della barriera cinetica occorrente per la formazione della struttura.
Quello che è emerso dai precedenti studi è l'individuazione di tre possibili strutture candidate ad essere specie attiva della catalisi: due ossidi di superficie, la ricostruzione p-(4×4) e p-(7×7) e l'ossido di bulk. L'obiettivo della mia tesi era quello di identificare quale delle tre specie si forma sulla superficie di argento alle condizioni di catalisi. La tecnica usata per raggiungere questo obiettivo è la Surface X-Ray Diffraction, che non necessitando di condizioni di ultra alto vuoto, permette di poter simulare le reali condizioni della reazione. Tale tecnica necessita l'uso di radiazioni con elevata brillanza, per questo motivo essa può essere adoperata solo nei sincrotroni. Il campione è stato

sottoposto, prima dell'esperimento, alle convenzionali procedure di pulizia superficiale in ultra alto vuoto. Inoltre, è stata verificata l'assenza di contaminanti sulla superficie tramite misure di spectroscopia Auger, mentre la qualità cristallografica superficiale è stata controllata con misure LEED. Tali tecniche e il *setup* per l'ultra alto vuoto usati, sono stati descritti nel Capitolo 2. Nel Capitolo 3 vengono descritti i fondamenti teorici delle Surface X-Ray Diffraction.
Per studiare la catalisi è stato utilizzato un reattore di flusso progettato dallo stesso staff della beam-line, adatto alle reazioni di catalisi eterogenea, che ha permesso durante l'esperimento sia di effettuare misure di SXRD ad alte pressioni, sia di portare il campione in condizioni di ultra altro vuoto per effettuare la procedura di sputtering e annealing. Durante l'esperimento le ricostruzioni indotte sulla superficie dall'ossidazione sono state osservate, e la loro stabilità al variare della pressione e della temperature è stata studiata. Nel Capitolo 6 vengono analizzati i dati sperimentali: quello che emerge è l'inadeguatezza della tecnica usata per questa superficie Ag(111), poiché il fascio sembra indurne l'ossidazione.

Chapter 1

Introduction

The oxidation of the silver surface has been studied strongly for over forty years. The reason for such determination, has to be searched in the industrial applications of this metal. In fact, although silver is a noble metal, its surfaces have the ability, under suitable conditions of pressure and temperature, to catalyse ethylene epoxidation. The product of such reaction, ethylene oxide, is one of the major chemicals industrially produced because it is an important intermediate for the synthesis of glycols and polyols[7]. The past researches were aimed to get a full comprehension of this catalysis reaction, with the purpose to obtain a more efficient and rational process. The fundamental issue is to understand why the silver surface is catalytically active for this reaction. In order to get responses, the structures present on silver surfaces after oxidation process need to be studied, to identify the active phase of the catalyst.
Despite the huge amount of studies of this topic, a fully characterization of this heterogeneous catalysis is still missing. The reasons of such failures, are first of all in the complexity of the reaction and then, in the experimental techniques used for the investigations. The main and most readily available techniques for the study of surfaces, are performed in ultra high vacuum conditions. The results of these experimental techniques, do not reflect the actual reaction conditions, namely high temperature and high pressure. This so-called *pressure gap*, has been recently bridged, thanks to the largely diffusion of synchrotron facilities, that allow the use of Surface X-Ray Diffraction as experimental technique to investigate surfaces, at high pressure ($\approx$ 1 bar) and high temperature.

1.1 Ethylene epoxidation

Ethylene epoxidation is a heterogeneous catalysis. It is the *partial oxidation* of ethylene to ethylene oxide, an epoxide, i.e. a cyclic ether with a three atoms ring.

$$C_2H_4 + \frac{1}{2}O \longrightarrow C_2H_4O \quad \Delta H = -25 kcal/mol (1) \tag{1.1}$$

Silver is the unique catalyst for this reaction, it decreases the activation energy and increases the rate of the reaction toward equilibrium, without being appreciably consumed. The main features of a catalyst are its activity and its selectivity. The property of activity, refers to the rate induced by the catalyst, that leads the evolution of the reaction toward the chemical equilibrium. The selectivity is defined as the percentage of the consumed reactants that forms the desired product [30] and represents the ability of a catalyst to choose one pathways, among different parallel reactions. The catalysis is in this case heterogeneous, because the catalyst is a silver single crystal, while the reactants and the product are in a gaseous phase. The reaction takes place on the silver surface. In order to increase the catalyst activity, the surface/volume ratio of catalyst must be maximised, therefore a top-down preparation of the silver reduces it in many nano meter-sized particles and an inert porous structure is used as support(Al_2O_3). The optimal conditions for this reaction are temperature about $(530 \div 550)$ K and an atmospheric oxygen pressure [30].
In addition to ethylene epoxidation, there is another competitive parallel reaction, that leads to combustion. Scheme shown in Fig.1.1. The Ethylene can react with oxygen to form carbon dioxide and water, i.e.*total oxidation*:

$$C_2H_4 + 3\,O_2 \longrightarrow 2\,CO_2 + 2\,H_2O \quad \Delta H = -340 kcal/mol \tag{1.2}$$

The total oxidation is favoured thermodynamically, as deduced by comparing the enthalpy change between the two types of oxidation. Moreover, combustion products can be also reached, starting from ethylene oxide.

$$C_2H_4O + \frac{5}{2}O_2 \longrightarrow 2\,CO_2 + 2\,H_2O \tag{1.3}$$

The fundamental role of silver is its reasonable selectivity for the partial oxidation of ethylene. This selectivity is 40% and can be improved, up to 90% , by using Chlorine species as inibitor[7][5], and alkali or alkaline earth promoters, as Cesium[30]. All the industrially produced ethylene oxide, is obtained by this direct oxidation process. This molecule and its main derivatives, are majority of the products of the chemical industry. The 70% of ethylene oxide is converted is ethylene glycol, which is produced by hydrolysis and used as engine antifreeze. The other important derivatives are alcohol ethoxylates, which are used as detergents and surfactans[30].

Mechanism of reaction Ethylene oxidation takes place on the silver surface, after its exposure to a gaseous mixture of oxygen and ethylene. The oxygen can be adsorbed on the

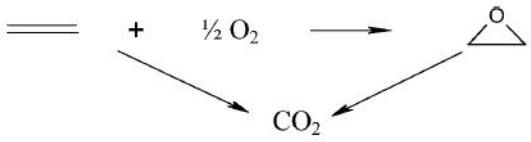

Figure 1.1: Scheme of the three competing reactions.Image from ref.[16].

silver in three different states, molecular dioxygen, adsorbed atomic oxygen, and subsurface atomic oxygen. The oxygen molecules are dissociated from the surface at higher temperature than 220K[7],[4], therefore they are not involved in this catalysis process. One of the first studies of the mechanism of ehtylene epoxidation, was made by Grant and Lambert[10],they demonstrated the fundamental role of an oxygen subsurface for the partial oxidation of ethylene. This subsurface of Oxygen is formed by the movement of the external adsorbed oxygen atoms, into subsurface lattice positions. The role of this subsurface, is to reduce the electron density of closer silver atoms. The external adsorbed oxygen atoms, that share bond with these silver atoms, become electron deficient oxygen $O^{\delta+}$ atoms. They strongly interact with the π electrons of the ethylene double bond, breaking it and so leading to the formation of ethylene oxide[7]. This study shows that the mechanism of this catalysis is more complicated than a simple surface adsorption phenomenum. Moreover the electrophilic oxygen has the role of active species.

1.2 $Ag(111)$ oxidation

Catalytic activity and selectivity depend strongly on the morphology, surface chemical composition, phase composition and the structure of solid catalysts[7]. Therefore, to understand and improve the selectiviy of the catalyst is necessary to know the structures present on the surface. Recent studies on other noble metals used as catalysts, such as Pt[12] and Ru[22], demonstrate that on their oxidized surface is formed a structure called *oxide surface*, that enhances the catalyst properties. This surface oxide might be the active phase of the catalysis. Surface oxides are ultra thin oxides, made of one metallic layer surrounded by two layers of oxygen, generally their structure is correlated with the relative bulk oxide of the element. They appear as, an oxygen-metal-oxygen sequence perpendicular to the surface plane[24]. Researches about this active phase, were made also for the (111) surface of silver. Many models of this surface oxide were proposed in the past years, but it is still unknown and under debate, the responsible one for the catalytic activity of silver.

1.2.1 Ag(111): the surface

Silver is a noble metal of the 4d group of transition metals, it crystallizes in the FCC structure with a lattice constant of $4,0853\mathring{A}$. The oxidation of the (111)oriented silver surface is the mainly studied. In a FCC crystal this surface has a lower surface energy and so it is the most stable. The formation of extended (111)oriented surfaces, was observed in real silver catalyst[23]. The (111)surface of a FCC crystal is a 2D hexagonal lattice, it is the most efficient way of packing atoms within a single layer. This plane exhibits a very small sticking probability for oxygen, equals to 10^{-6}, even when it is atomically clean. Therefore, Ag(111) crystal surface is important, because is created with the greater probability but at the same time it is the most difficult crystal face to oxidize.

1.2.2 History of Ag(111) oxidation since 70s

In this section, the most significant studies about the structures formed on the silver oxidized surface, are briefly summarized. All these past studies, are based on expermental techniques performed in Ultra High Vacuum, as Scanning Tunneling Microscopy, Low Energy Electron Diffraction and Temperature Desorption Spectroscopy.

First model of surface oxide: O-$p(4 \times 4)$-Ag(111) The $p(4 \times 4)$ reconstruction, was the first oxygen induced structure considered responsible for the catalytic activity of silver during epoxidation of ethylene. It was studied intensily and in last years, many models for this structure were proposed. The first model was proposed by Rovida et al. [29] in the 70s. The surface was oxidized with molecular oxygen at high pressure(up to 1.33 mbar) to obtain an appreciable coverage of oxygen atoms on the surface. LEED measurements have revealed the presence of a reconstruction with an unit mesh, having a dimension four times bigger than the bulk one. The interpretation of Rovida was that the reconstruction was a thin layer of Ag_2O in the (111) direction. The Ag_2O is the most stable silver oxide, it crystallises in the cuprite structure with a lattice constant of 4,72Å. Ag becomes Ag_2O thanks to the inclusion of two oxygen atoms in the FCC unit cell, at one quarter of the tetrahedral sites. Between the lattice formed by a (111) plane of Ag_2O and the (111) plane of the Ag, exists a coincidence: the size of its unit cell in (111)direction is four time the size of the Ag (111) unit cell Fig.1.2.a) and this was the key information to build his model. A decade later, Campbell[4] by the use of various surface science techniques, as LEED,TDP and XPS, proposed a new model: a three layer of $Ag_2O(111)$ rotated by 30 degrees relative the unit cell of the bulk. Also the thickness of the thin film of Silver oxide was measured, it was approximately $14\mathring{A}$ [4].

Subsequently, with the support of STM measurements and DFT calculations, the O-$p(4 \times 4)$ model was optimised. A new proposed model was the $Ag_{1.83}O$[6] shown in

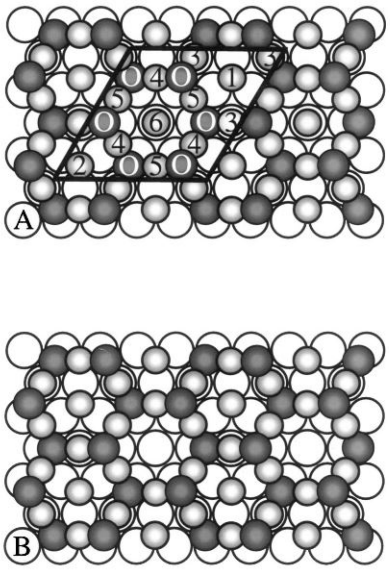

Figure 1.2: a)Model of the trilayer of Ag_2O reconstructed on Ag(111). Light gray and dark gray spheres correspond respectively to Ag and O atoms in the trilayer. Instead open circles represent the Ag(111)surface. The unit cell of the trilayer is marked. The same numbers indicate atoms of Ag that are symmetrically equivalent. b)$Ag_{1.83}O$ model. Obtained by removing the central Ag atom in a third of the hexagonal Fig.from ref.[6].

Fig.1.2.b), with a $Ag_{11}0_6$ stoichiometry. This structure consists of hexagonal rings, shown in Fig.1.3, constituted by an alternating sequence of silver and oxygen atoms (O-Ag-O sequence). The proposed $Ag_{1.83}O$ model was an Ag-deficient version of the Rovida-Campbell trilayer model. Finally, this model was improved by density functional theory calculations. The new model, more stable than the previous one, is the $Ag_{1.33}O$, with a Ag_9O_6 stoichiometry. This structure is obtained by removing all central Ag atoms from the Rovida-Campbell trilayer model .

This reconstruction was observed sperimentally with STM images,fig.1.3 and its stability at 400K was predicted by theoretical calculations (DFT calculations)[24]. The missing piece of past researches is to check sperimentally its stability under industrial conditions and verify the model with a crystallography method.

1.2.3 Near ambient oxidation of Ag(111)

In order to check the stability of the $p(4 \times 4)$ reconstruction during the catalysis, the reaction conditions must be simulated. The experimental technique suitable for this purpose is the Surface X-Ray Diffraction. It allows an in-situ measurement at real pressure and temperature conditions, filling up in this way the so called *pressure gap*. SXRD was used for studing the oxidation of Ag(111), for the first time by Schmid et

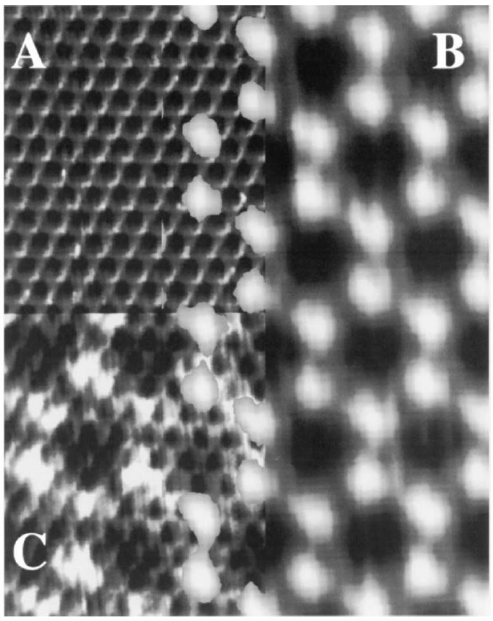

Figure 1.3: Scanning tunnelling microscopy images. a)STM image with inverted contrast of the clean $Ag(111)$ surface. b)High resolution STM image and c)STM image of the O-(4×4) reconstruction with an honeycomb structure.Image from ref.[6].

al.[31]. One of the most striking results of this research, that combined SXRD with LEED, STM measurements and DFT calculations, was the development of a new model for O-$p(4 \times 4)$, that allowed to discard the previous ones. The use of SXRD showed the incompatibility between SXRD measurements and STM data of O-$p(4 \times 4)$ models based on the O-Ag-O trilayer structure. The new proposed model is the Ag-Adatom-Trimer model[31]and consists of two Ag_6 nano triangles, located, one in the fcc site and the other in the hcp[31], Fig.1.4. These silver triangles are interlinked by oxygen atoms. The study of this surface by the use of SXRD[24], also allows to measure in-situ the stability diagram of the O-$Ag(111)$ system, varying the temperature from 473K to 723K and the oxygen pressure from UHV up to 2 bar . In Fig. 1.5 is shown the stability diagram. With this measurement was possible to observe which phases are stable at different temperature and pressure conditions. In particular, three phases were investigated: a clean silver surface, a disordered chemisorbed oxygen and the O- $p(4 \times 4)$ reconstruction. The clean silver surface was demonstrated of being stable only at low temperatures and low pressures, an increasing of the oxygen pressure carries to a dissociative process of the chemisorbed oxygen. After a further increase of the oxygen pressure, the formation of $p(4 \times 4)$ reconstruction was observed. As we can see from the stability diagram, the $p(4 \times 4)$ reconstruction is stable at 523 K and 2 bar, which are the catalytic condition for ethylene epoxidation.
A subsequent study, demonstrates the presence on the surface, during the oxidation of Ag(111), of a competitive growth among several oxygen induced structures[23]. $Ag(111)$

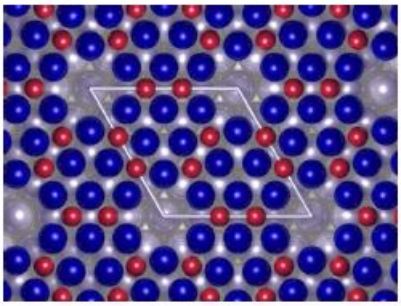

Figure 1.4: Ag-Adatom-Trimer model. Red spheres are oxygen atoms and blue ones are the Silver atoms. Image from ref.[24].

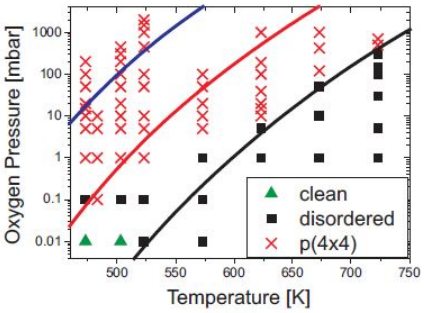

Figure 1.5: Stability diagramm of the O-Ag(111)system.Image from [24].

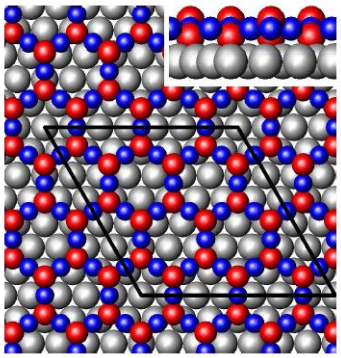

Figure 1.6: $p(7 \times 7)$ structural proposed model.Visions from above and side are shown. Silver atoms are represented by blue spheres and oxygen by the red ones.Image from[23].

surface was oxidated at extreme conditions,(i.e. 1 bar of oxygen and at 773K) and at the same time, it was investigated by SXRD and was observed a competitive growth among three different structures: the well known $p(4 \times 4)$, a $p(7 \times 7)$ reconstructions and bulk oxide. This was an unexpected result, because all the previous UHV studies considered only the $p(4 \times 4)$ as candidate species for being the active phase of the catalyst. The $p(7 \times 7)$ structure exhibits the honeycomb structure on the $Ag(111)$ surface and the model proposed in this study for this reconstruction is based on a three-layer O-Ag-O slab of Ag_2O, the same of the surface oxide. This was suggested by the almost perfect fit (1% of mismatch) between 3 unit cells of the (111) surface of silver oxide strucure and 7 unit cells of $Ag(111)$. The model is shown is Fig.1.6. The stoichiometry of this layer is Ag_9O_6, this corresponds as said in the previous section, to the most stable surface oxide layer on Ag(111). The studies of bulk oxide structure demonstrated that under the extreme condition of the experiment a new formation process of Ag_2O should be considered, the Stranski–Krastanov growth mode. This epitaxially growth consists in an inverted stacking of Ag planes compared to the standard cuprite structure of silver oxide. The standard and inverted sequences are shown in fig 1.7. Furthermore, SXRD measurements provided evidence of the formation of bulk islands instead of a complete coverage. In conclusion, the use of this surface technique allowed to deepen the knowledge on what happens to the surface of silver during oxidation at higher temperature and high pressure. From all the proposed models, only the $p(4 \times 4)$, the $p(7 \times 7)$ and the bulk oxide are stable under the catalytic conditions. These structures have shown a competitive growth and led to speculate that not only the $p(4 \times 4)$ reconstruction could be responsible for the catalytic action of silver, but also these new proposed models.

1.2.4 Recent research

In one of the latest studies [9] it was investigated how the surface oxygen-induced structure on $Ag(111)$ changes depending on oxygen gas flux and its incident energy. The

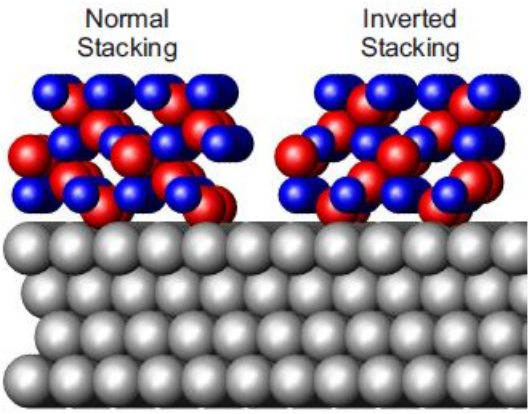

Figure 1.7: $Ag_2O(111)$ suface sequences on $Ag(111)$.Silver atoms are shown as blue and oxygen atoms as red spheres.Image from[24].

sample was undergone to extreme conditions, to simulate the actual reaction condition with the aim of reproducing the same structures which are formed during catalysis. Therefore, the surface was exposed to an higher dose of oxygen, higher flux and higher energy. The experimental techniques used in this case were the TDP and STM. The STM image of the surface after this extreme exposure in shown in fig.1.8B). In this conditions no subsurface of oxygen is formed, on the contrary as shown in the STM image, a disordered and rough surface appears. In the fig.1.8A), is shown, as a comparison, an STM image of large and ordered domains of the $p(4 \times 4)$ reconstructions, obtained in this case with gently conditions of exposure, i.e. low energy and low oxygen gas dose. In conclusion, what emerged from this research is the heavy dependence on the exposure conditions, of the structures formed on the surface $Ag(111)$. As catalysis of ethylene epoxidation takes place at high oxygen pressure condition what can be hypothesized is that the subsurface of oxygen is not longer the necessary phase for the activation of silver surface, but it may be the bulk oxide.

Conclusions

Silver catalyzed ethylene epoxidation has been studied for over forty years and to this date the mechanism of this reaction is still under debate. We know for sure, that the active catalyst, is not metallic silver and neither a simple O-Ag adsorption system, but an oxidized silver surface that enables the partial oxidation of Ethylene. The identification of this active surface structure is still under research. The main candidates are O-$p(4\times4)$, O- $p(7 \times 7)$ and bulk oxide. It was demonstrated that these structures are stable under the catalytic conditions by the use of Surface X-Rays Diffraction, but it is still unknown which one among these is the active phase. Anyway, a last step for a faithful simulation of the ethylene epoxidation condition is missing, because the surface should be exposed

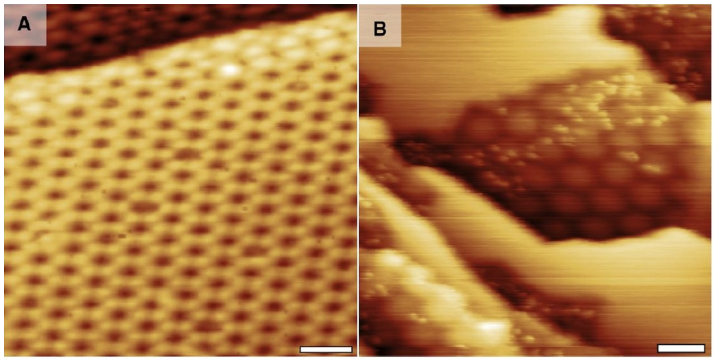

Figure 1.8: STM images: A)Reconstruction after gently conditions of exposure: large domains of $p(4 \times 4)$ structures on $Ag(111)$. Scale bar =2 nm. B) highly corrugated $Ag(111)$ surface after extreme conditions of exposure.Scale bar = $5nm$,Image from [9].

to a mixture of molecular oxygen and ethylene.

Chapter 2

Experimental techniques

In this chapter is introduced the UHV technology, namely the UHV equipment and the standard UHV experimental techniques for probing the surfaces, as Low Energy Electron Diffraction (LEED) and Auger Electron Spectroscopy (AES). Ultra High Vacuum condition, i.e. pressure $< 10^{-9}$ mbar, is necessary for a preliminary characterization of the catalyst's surface. From LEED and AES experiments the informations of, respectively, crystallographic perfection and cleanliness of the surface can be deduced.

2.1 Sample preparation and characterization in regime of UHV

In order to obtain a correct characterization on an atomic level of surfaces, is necessary to ensure that the surface composition remains unchanged during the experiments. A solid surface is an interface between condensed matter and the air. Atoms and molecules in the atmosphere that impinge on the surface, can be adsorbed and form strong bond, i.e. be chemisorbed or they can form weak bond and be thus physisorbed. For this reason, real surfaces under atmospheric pressure are far from an ideal and well-defined systems. Adsorption at the surface depends by the gas pressure and by the sticking coefficient of the surface. This last, is the ratio between the number of molecules that are adsorbed after an hit and the total number of collisions at the surface in the same time intervall. The worst case for the maintenance of a clean surface is when this coefficient is equal to 1, i.e. at each collision we have adsorption. Consequently, exists a characteristic time intervall τ, during which, on the solid surface a monolayer of contaminants is formed. This time interval τ, if the sticking coefficient is equal to 1, is equivalent to the ratio between the number of atoms on the surface and the number of collisions at the surface in the unit time [3].

$$\tau = \frac{A \cdot \rho_s}{A \cdot < v > \cdot \frac{n}{2}} [3]$$

where A is the considered surface, ρ_s is the density of the material at the surface and then, their product is the number of atoms at the surface. At the denominator , the product represents the number of molecules that will hit the surface A. This is the product of the surface A for the average velocity of the molecules, it gives a volume for unit time. Finally the multiplication for the gas density n will give the number of molecules in this volume. The $\frac{1}{2}$ factor represent the assumption that only half of them will go in the correct direction for hit the surface. In particular, if we consider a metallic surface with ρ_s equal about to 10^{15} $atoms/cm^2$ exposed to atmospheric pressure, τ is equal to 4 ns[3]. Thus, if we considered a surface with sticking coefficient equal to 1, exposed to atmospheric pressure and at room temperature, we will have the formation of a monolayer of contaminants on the surface in this very short time intervall. In order to increase this time τ, the density of the gas and the average velocity should be decresed. This is obtained decreasing the gas pressure. If the pressure is very low, in the range that is called "Ultra High Vacuum" i.e. $p < 10^{-9}$ mbar, the time to form a monolayer of contaminants becames in the orders of hours. In conclusion, for the characterization of a surface the pressure should be maintained in this UHV range.

2.1.1 UHV setup

The UHV equipment consists in a chamber maintained in the regime of Ultra High Vacuum, inside which is inserted the sample. Such low value of pressure is achieved by

the use of pumps. Whereas the pressure should be changed of 13 orders of magnitude, from atmospheric $p = 10^3$ mbar to UHV $p = 10^{-10}$ mbar, different pumps are necessary [21]. Generally, scrool pumps or rotary pumps are used as "backing pumps" for more powerful pumps[21]. These support pumps, pump the system from atmospheric pressure untill cover a range of pressure that is $10^{-2} \div 10^{-3}$ mbar. Then, the UHV regime is reached thanks to powerful pumps like ion, turbomolecular or cryopumps[17]. For isolating sections of the vacuum system, valves are used. For example, for separate the pumps from each other and from the chamber. A particular attention should be gave to the materials used for the valves, sealing gaskets and vessel of the chamber. Plastics materials are not suited for gaskets because they can't resist to high temperature, so they are usually made by Copper. Inside the chamber, materials without outgassing properties have to be used [20]. Then, Zinc and Cadmium are forbidden [21] and so the mainly used materials are Tantalum, Molybdenum and stainless Steel. Before starting with the pumping process, the entire equipment that was exposed to the air has to undergo to a bake-out process. It consists in a heating of the system at $423 \div 453$K for about 10 hours[17]. This process, causes the desorption of the molecules of water that covered the inner walls of the set up. The water molecules have a high dipole moment and for this reason they stick easily on the surfaces when they are exposed to air.[17].
The pressure inside the chamber is monitored with different types of pressure gauges. The types used are, the capacitance manometers, Pirani gauge and the ionisation gauge [19]. Each of these pressure gauges is able to measure the pressure in a restricted interval of pressure. In particular, the capacitance manometers covered the higher pressure interval, from atmospheric untill 10^{-3} mbar[17].In this type of gauges the variation of pressure are measured with a volume changes respect to a reference one, thanks to the deformation of a separation membrane [17]. To quantify this volume variation, the electrical capacitance between the membrane and a fixed plate[19]is measured. The other gauge used in the pressure range of $0.5 \div 10^{-3}$ mbar [19], is the Pirani gauges. It consists in a Tungsten filament, heated by a fixed current. In this case, what is measured is the resistance of the filament, by a Wheastone bridge[19][17]. The resistance depends also from the temperature. How the filament losses thermal energy depends on the thermal conductivity of the gas. This latter, is proportional to the gas pressure[19]. Finally, the Ionization gauge is used for operate in the range below 10^{-3} mbar[17]. The one used in the Laboratory, is the Bayard-Alpert Gauges type, because it is the most suitable for UHV conditions [19]. This gauge correlates the measurement of the fixed emitted current from an heated filament and the current measured in the collector (Anode). This collected current depends on the ionization rate of the gas by the emitted electrons, that increase with the gas pressure[17]. Finally, an usefull instrument, often present in a UHV equipment, is the Residual Gas Analyzer (RGA). It allows to monitor in real time the gas composition inside the chamber, thanks to a quadrupole mass spectrometer.

2.1.2 Cleaning procedure

Before the installation inside the UHV chamber the sample undergoes to a set of preparation treatments. The first is the polishing procedure. It is an abrasive process, in which the topmost layer is removed using hard grains. The procedure occurs in steps, in each of which the size of the grains is reduced. The aim of this method is to obtain a flat and well oriented surface. After that, the sample is inserted in the UHV chamber and there cycles of sputtering and annealing are made. These are cleaning procedure performed in UHV conditions. Sputtering process consists in a ion bombardment. A noble gas (as Ar, Ne, etc), is ionized by the electrons generated by the ion gun. Then, these Ions are accelerated by a potential toward the sample. The impact removes the topmost atomic layers of contaminants. After that, annealing of the sample is necessary in order to remove the noble gas ions stuck in the surface and to restore the surface crystallinity, destroyed by the bombardment[17]. The annealing temperature depends on the material, in general it should be maintained under a 20% of the melting temperature. The purpose of this process is to obtain the desorption of the impurities embedded in the surface. Sometimes, during the heating of the sample, the impurities from the bulk diffuse towards the surface[17] and for this reason many cycles of sputtering followed by annealing are recommended. The Sputtering and annealing procedure is repeated untill the surface reaches the degree of cleanliness and crystallographic order desidered. For checking these properties of the surface, Low Energy Electron Diffraction and Auger Electron spectroscopy are used. Both of these experimentals are performed in UHV regime.

2.2 LEED

Low Energy Electron Diffraction is used as a standard technique to investigate the crystallographic quality of a surface. The physical phenomena at the base of this experiment is the Diffraction. The crystal is probed by a beam of low energy electrons, the backscattered ones from the atoms of surface behaves like waves and interfere. The result is a pattern of diffraction spots. The typical electron energies for LEED are in the range of $50 - 300$ eV[17]. From the relation of De Broglie $E = \frac{h}{\lambda}$, knowing the energy of the electrons we can derive the wavelenght of the electron waves. In this range of energies, the λ is equal about to $\simeq 1\mathring{A}$. The electron waves, thus have a λ comparable with the intaratomic distance in the crystal lattice and therefore the conditions for having diffraction is satisfied. LEED is particularly suited for surface studies, since the mean-free path of these low energy electrons in the solid is short enough to give good surface sensitivity. In Fig.2.1, is shown the mean free path of an electron that propagates in matter as a function of its energy. This physical quantity provides an estimate of the penetration depht of the electrons and depends mostly by the electron energy, for this reason is considered a "quasi-universal" curve, i.e. is the same for all materials [3]. For the typical energy of the LEED this path is equal to $5 \div 9\mathring{A}$. Therefore, only few $(2 \div 5)$

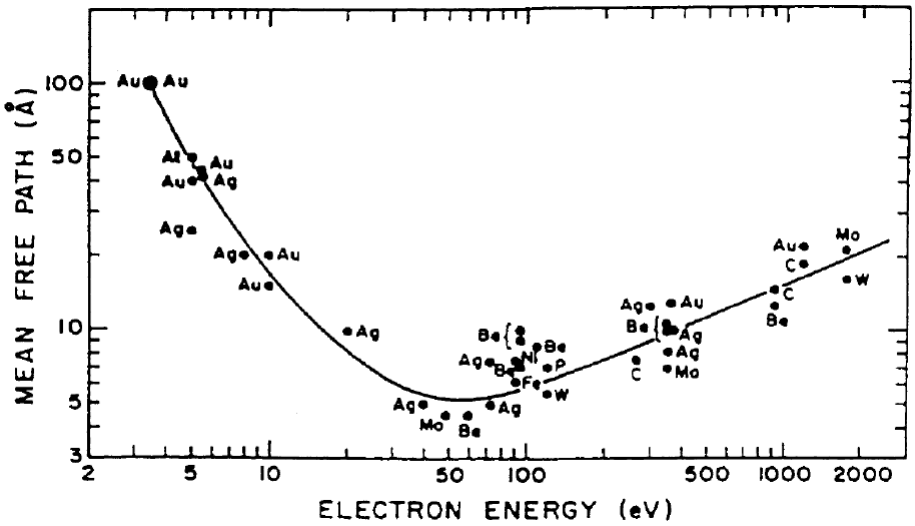

Figure 2.1: Anelastic mean free path for electrons in function of their energy. This curve is almost universal for all materials. Image from [3].

monolayers are probed by this experimental technique.

2.2.1 Basics of Diffraction from a Crystal lattice

The physical phenomenum of Diffraction from solid state matter, permits to make a full analysis of the crystal structure of the material. The diffraction is the results of the scattering of the waves by the atoms in the matter and of their consequently inteference. These waves can be electrons, photons or others particles, the important thing is to select the correct energy for having a wavelenght comparable with the interatomic distance in the studied material. The theory of diffraction was developded by Bragg and Von Laue. Their formulations of the Diffraction theory are different but equivalent[1]. In the Bragg's theory, the crystal is considered as a ensable of parallel planes of ions. The distance between the planes is constant and is equal to d. The X-rays are scattered by the planes. In this theory is based on the assumption of a specular geometry, then the angle of incidence of the X-rays is equal to the outgoing one $\theta_{in} = \theta_{out}$, i.e. the X-rays are reflected by the planes. The conditions for Diffraction, is that the path difference between two X-rays reflected from different planes, highlighted in red in the Fig.2.2, is equal to a multiplier integer of the wavelength [1].

$$n \cdot \lambda = 2 \cdot d \cdot \sin(\theta) \qquad\qquad Bragg's \quad law$$

In the Von Laue theory, the matter is considered as a crystal lattice instead of an ensemble of parallel planes. The X-rays are back-scattered by the atoms or by the ions placed in the points of the Bravais lattice. They are identify by the vector $\overrightarrow{R}$. The

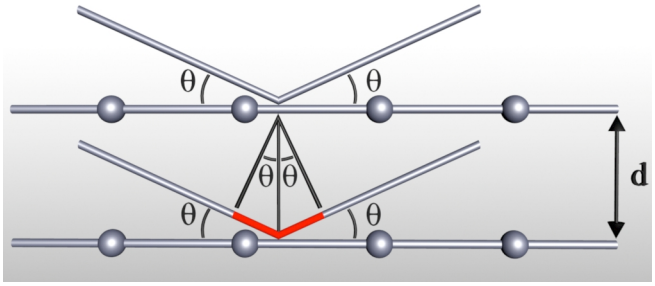

Figure 2.2: Bragg Theory: The incident waves are reflected by a family of planes. The angle of incidence is θ and the distance between the planes is d. The path difference between the two backscattered waves is highlighted in red and for having diffraction it should be an integer multiple of the wavelength.

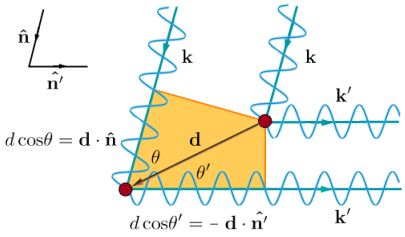

Figure 2.3: Von Laue approach
Von Laue Theory: in this case the centres of scattering are the atoms placed in the positions of the bravais lattice. The path difference is $d \cdot \cos\theta + d \cdot \cos\theta'$. Image taken by[14].

condition for having diffraction is always, a constructive interference of the backscattered waves. In this case, considering the geometry shown in Fig.2.3, the difference path is :

$$\overrightarrow{d} \cdot (\overrightarrow{n} - \overrightarrow{n'}) = m \cdot \lambda$$

where $\overrightarrow{n}$ and $\overrightarrow{n'}$ are the directions of incident and scattered rays. Multiplying it for $2\pi/\lambda$ (the scattering is elastic), we find the relationship for the wave vectors:

$$\overrightarrow{d} \cdot (\overrightarrow{k} - \overrightarrow{k'}) = 2\pi \cdot m$$

The next step is considering all the waves scattered. The condition for constructive interference should be satisfy for all of them [1]. Each of these scattered at the points of the Bravais lattice, than the equation should be verify for all the value of the vector $\overrightarrow{R}$.

$$\overrightarrow{R} \cdot (\overrightarrow{k} - \overrightarrow{k'}) = 2\pi \cdot m$$

If I take the complex exponential, I obtain:

$$e^{i \cdot (\overrightarrow{R} \cdot (\overrightarrow{k} - \overrightarrow{k'}))} = 1$$

This last equation is the definition of the vectors of the Reciprocal Space[1],shown in the following:

$$e^{\overrightarrow{R} \cdot \overrightarrow{G}} = 1$$

Where $\overrightarrow{G}$ is the generator vector of the reciprocal space. The Von Laue condition explains the Diffraction theory, using the concept of reciprocal space, in particular the difference between the wave vectors of the incident and scattered waves should be equal to a vector of the reciprocal space of the Bravais lattice of the material.

$$\overrightarrow{k} - \overrightarrow{k'} = \overrightarrow{G_{h,k,l}}$$

A method for visualizing the Von Laue condition, is the Ewald construction. It consists in a sphere drawn in the reciprocal space of the crystal. For drawing the sphere, the incident wave $\overrightarrow{k}$ vector is drawn starting from the origin of the reciprocal space. The tip of this vector will be the centre of the sphere, that will have a radius equal to $\| \overrightarrow{k} \|$. After that, the sphere is drawn, shown in Fig.2.4. The diffraction will occur only if the sphere will cross the points of the reciprocal space, in particular ad every crossing will correspond a Bragg peak i.e., a maximum in intensity. Only these crossing points of the reciprocal lattice and Ewald sphere will fulfill the Laue condition. Therefore, from the spatial distribution of diffracted beam can be deduced the crystal structure[1].

[1]The reciprocal Space is a Bravais lattice, it is built from the direct lattice and represents its Fourier transform. It is constituted by all wave vectors that have physical meaning for the direct lattice. Each of the vectors of the reciprocal space is perpendicular to a family of planes in the direct space[1]

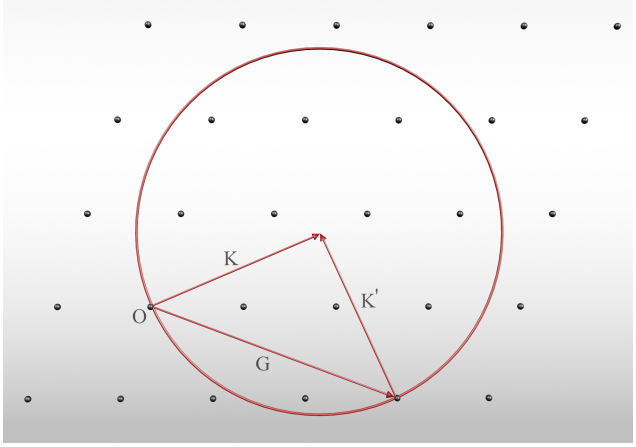

Figure 2.4: Ewald construction: the points are the reciprocal space and the vectors represent the incident wave vector $\overrightarrow{k}$ and the outgoing vector $\overrightarrow{k'}$. The condition for having diffraction is that the sphere built starting from these vectors, crosses the points of the reciprocal space.

2.2.2 Diffraction theory for LEED

As said in the previous paragraphs, LEED probes few monolayers of the sample, as a consequences is considered a superficial experimental technique. Then, we have to consider a diffraction from a 2D surface. In this case, the periodicity of the lattice is broken in the perpendicular direction of the surface. Then, the Von Laue condition should be satisfy only for the components of the wave vector parallel to the surface[17]. The wave vector can be decomposed in two components, the one parallel to the surface and the one perpendicular:

$$\overrightarrow{k} = \overrightarrow{k_{\parallel}} + \overrightarrow{k_{\perp}}$$

Therefore, the condition to fullfill for having diffraction is:

$$\overrightarrow{k_{\parallel}} - \overrightarrow{k'_{\parallel}} = \overrightarrow{G_{h,k}}$$

This above is the momentum 's conservation law and in this case, interests only the wave vector components parallel to the surface[21]. Their difference vector have to be a vector of a 2D reciprocal lattice $\overrightarrow{G}_{h,k}$, where h and k are the miller's indeces. Instead the perpendicular component at the surface $\overrightarrow{k_{\perp}}$, must satisfy any condition[17]. In order to extend the well-known Ewald construction to a 2D system, the conservation condition for the perpendicular component of the wave vector have to be relaxed. Then, instead of having the point of the reciprocal space, we will have rods (as shown in Fig.2.5). Each of them, will be perpendicular to the surface and identified by (h,k) Miller's indeces. The rods represents the fact that the third index of Miller l, can assume all the values because it has no conditions to satisfy. Now, we have peaks of diffractions every time

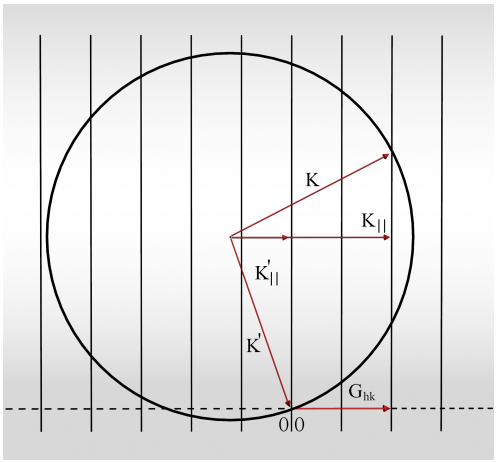

Figure 2.5: Ewald construction: diffraction from a surface
Ewald construction in the case of a diffraction from a Surface. Instead of points, rods are presents. Now the condition of conservation of the momentum concerns only the parallel component of the wave vectors.

the Ewald sphere will cross a rod. In this case, the pattern of diffraction is ensured for every energy of the incident beam and for every angle[17]. This is due to the fact that, instead of the points of the reciprocal space, i.e. a discrete pattern, we have rods.

2.2.3 LEED pattern

LEED measurements record the diffraction peaks due to the scattering of a low energy electron beam from a crystal lattice. As, the only scattering considered is the elastic one, the informations gained by these measurements are about the symmetry and the geometric arrangement of atoms [17]. As said previously, these informations refer to more superficial layers of the solid. A LEED measurement consists of sharp spots in contrast with a low background intensity. These spots represent the reciprocal space of the crystal lattice studied. From a simple observation of the geometrical position of the spots, the symmetry of crystal lattice can be obtained. Instead, in order to know the atomic arrangement at the surface, is necessary make an intensity measurements of the peaks. Others fundamental informations can be deduced, for example the presence of defects, as a non well-flat surface or the presence of disordered adsorbated atoms or a superlattice, namely a reconstruction over the surface.In this last case, another pattern of less intense spots appears. The rotational alignment among the unit cell of the superlattice and the substrate unit cell can be observed from the measurement. Finally, the quality of the surface is reflected in the pattern. In fact, defects or crystallographic imperfections will broaden the spots and increase the background intensity[17].

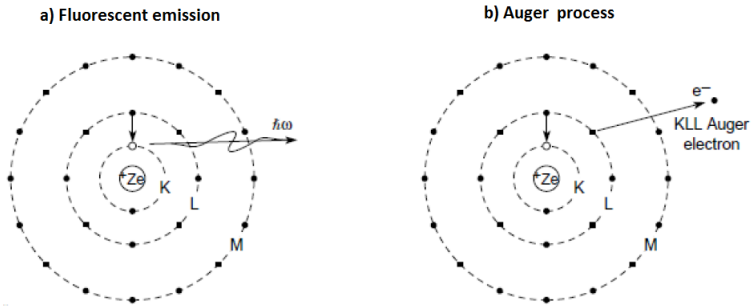

Figure 2.6: Intra atomic de-excitation process. a)Fluorescent proces: it consists in a transition of an higher energy electron to the core level and the consequently emission of an X-ray. b)Auger process: it is a non-radiative de-excitation process. In this case the energy gained by the transition of the L-electron to the core level, is transferred to another L-electron that is emitted. Image from [3].

2.3 AES

Auger Electron Spectroscopy is an electron core-level spectroscopy[17] and it is based on the Auger process. This last, is an intra-atomic process of de-excitation. In this experimental technique, atoms are excited by a a primary electron beam, produced by an electron gun with typical energies of $2 \div 5$ KeV[17]. The electron beam interacts with matters and it may create holes in the core level of the atoms. Then, the excited atoms can relax with a radiative process (Fig.2.6.a)) or with a radiation-less de-excitation, thus with the emission of Auger electrons(Fig.2.6.b)). In this last process, the Auger electron gains the energy for being emitted by the transition of another electron, that starting from an higher level fills the initial vacancy in the core level. The Auger process are labeled with the name of electronic shell involved in the transition [17], for example KLL process or LMM process. The two processes of de-excitation, shown in Fig.2.6 are competitive. In particular, the Auger emission is more probable for atoms with low atomic number when the hole is in a deep core level, like a K shell. Otherwise, if the hole is in a less deep level, like a L shell, the Auger process became more probable for atoms with higher atomic number. The radiative process has the opposite trend [3]. Since, the kinetic energy of the emitted Auger electron is directly related to differences in core-level energies, its measurement, can be used to identify a particular element[17]. For example, for the KL_1L_2 process:

$$K = E_K - E_{L_1} - E_{L_2} - \phi$$

Where ϕ is the work function of the material. Therefore, this experimental techniques is used for determine the surface chemical composition of the studied material. The measurement consists in a spectrum, i.e. a measurement of the number of emitted

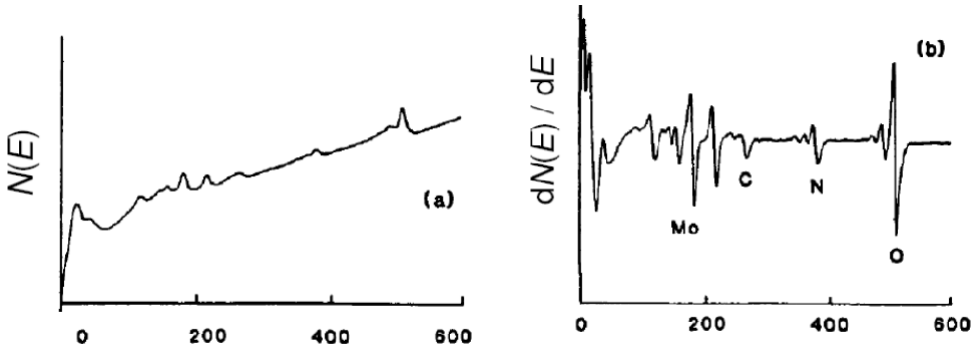

Figure 2.7: Images from [3]. a)Direct Auger electron Spectra.b)Auger Spectra acquired in the derivative mode.

electrons as a function of their energy. The energies of the Auger electrons are in a range of few tens of eV, to a 3 keV. As discuss in the previous paragraph, the electron mean free path λ depends only by their energy, from img.2.1 we can deduce that in this case λ in the range of $(10-30)\mathring{A}$ [17]. The probability that the Auger electrons can escape from a depth d, decays exponentially and then, at a depth of some λ the escape probability for the Auger electron becomes very small. It means, that this experimental technique is very sensitive to the surface, because the emitted Auger electron emerged from fews layers under it. For having a correct study of the surface composition, the Auger Electron Spectroscopy needs UHV condition. The Auger signals are smaller signals respect to a background of Secondary electrons. These last, are electrons that emerges from the matter at low energy ($E < 50eV$)[3]. They could be electrons from the incidence beam that lost their energy and reversed their trajectory, due to their inelastic scattering with the atoms. They could be also, photoelectrons emitted from atoms after the absorption of the bremsstrahlung[2] radiation. In order to suppresse this background of secondary electrons, the Auger Spectra are usually registered in the derivative mode (Fig.2.7b)). Then, instead of classical peaks, we have a signal with a positive peak following by a negative one, as shown in Fig.2.8. The energy of the minimum of the derivative spectrum is used to identify the chemical elements, despite it corresponds to the steepest slope of N(E) and not to the maximum of the Auger peak. More over the Auger spectrum, may also contains information on the chemical bonding states of the atoms, e.g. the changing of the chemical environment is reflected in a change of the Auger peak position or in its shape.

[2]It is the radiation emitted by the electrons of the primary beam, after their deceleration due to attractive force generated by the electric field of the positive charged nucleous. In general, it is the electromagnetic field emitted by a charged particles after its deceleration. This emitted radiation has a continuous spectrum in the range of X-rays.

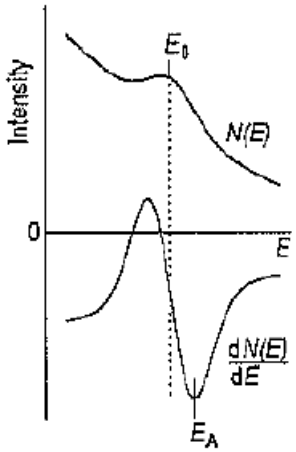

Figure 2.8: Image taken by [21]. It represents first the Auger peak in the direct acquisition and below the peak in the differential mode. Here is clear that the energy value of the minimum corresponds the steepest slope of the direct Augur peak.

Chapter 3

Surface X-Rays Diffraction

3.1 Introduction

Surface X-Rays Diffraction was used since the 80s for the study of the crystal structure of surfaces and interfaces[34]. In this experimental technique, an X-rays beam interacts with matter, in particular it is scattered during its propagation by the electrons of the atoms in the crystal lattice. These scattered waves, interfere and give rise to a diffraction pattern. From the study of this pattern, the crystallography of crystals can be derived. For the study of surfaces, a very intense source of X-rays is needed because the scattered intensity from a surface is million times less intense respect to the bulk one [34]. The signal from the surface comes from about 10^{15} atoms and it have to be measurable respect to the bulk signal, that comes from about 10^{23} atoms [17]. Therefore, in order to be able to measure this signal from the surface, is necessary a powerful source of X-rays. As a consequences, this kind of experimental technique is necessarily performed in the Synchrotron facilities. Before the theoretical discussion of the SXRD, the properties of X-Rays are discussed in the following paragraph.

3.2 Properties of X-Rays

X-Rays are electromagnetic radiation, their wavelength is defined in a range between the ultraviolet light and the gamma rays. The wavelength interval used for determining the crystallographic structure of matter is $(0.5 \div 2.5)\mathring{A}$, known as "hard X-rays" [11]. This interval of λ is chosen because these are the typical interatomic distances in solid state matter. One of the most important properties of X-rays, is the value of their index of refraction. It has always a value slightly lower than one for all solid medium.

$$n = 1 - \delta \quad where \quad \delta = (10^{-4} \div 10^{-5})[11]$$

This means that their propagation velocity inside the medium doesn't change from the speed of light in the vacuum. Then, X-Rays are not refracted by solid matter and so they can't be focused by lens. As regards their interaction with matter, during the propagation they are attenuated in intensity. One of the reasons of this phenomenon, is the scattering of the beam by the eletrons of the atoms in the lattice. This process causes a deviation in their trajectory. It could be elastic or not. A characteristic of the X-Rays propagation in matter, that distinguish X-Rays from, for example electrons, is low value of scattering cross section. This physical quantity represents the area around the atoms that scattered the radiation. Lower is this value, more deeply penetrates the beam without deviation of its trajectory. This property allows to apply the kinematic scattering theory [1] for the X-rays propagation inside matter. The other process that causes the decreasing of X-rays intensity during the propagation, it's their absorption by the atoms. In particular, X-Rays photons energy are suited for being absorbed by atoms that then can return to the ground state with one of the de-excitation process saw in the previous chapter. The intensity decreases during the propagation with an exponential trend. It follows the well-known Lambert-Beer law:

$$I(x) = I_0 e^{-\frac{\mu}{\rho}\cdot\rho\cdot x}$$

where μ is the absorption coefficient and ρ is the density of the material. This quantity $\frac{\mu}{\rho}$ is characteristic for each material and it depends also from the beam energy. Its value decreases with the increase of photon energy [3]. In conclusion, from the properties of X-Rays derive that the Surface X-rays Diffraction has advantages respect to others experimental techniques used for the study of the surface crystallography. First of all, the use of X-Rays as probe allows to consider valid the Kinematical theory. Instead, in LEED, where electrons are used for probing the surface, the multiple scattering theory has to be considered [34]. As said in the previous chapter, electrons have an high scattering cross sections, higher than the X-Rays one[34]. The kinematic approximation makes the SXRD data analysis simpler than the LEED one, therefore SXRD is favored for the study of complex surfaces[34]. The other advantage of SXRD than LEED, is the possibility of performing the experiment at atmospheric pressures. The reason of this, is the high penetration depth of X-Rays, consequence always of the low value of scattering cross section that has the matter during X-Rays propagation. Instead a disadvantage of SXRD, is the necessity of a synchrotron facility as X-Rays source. On the contrary, LEED required a simpler set up[34].
In conclusion, the importance of this experimental technique increased during the last decades because these properties makes SXRD suited for the the structures analysis of complex surfaces and for monitoring chemical reactions catalysed by crystal solid surface.

[1] Also known as Born approximation. It is a semplification on the Dynamical X-Rays Scattering Theory. It considered only single event of scattering.

3.3 Theory of Diffraction for X-Rays

As said in the previous chapter, in order to have diffraction, the radiation wavelength has to have the same order of magnitude of the interatomic distance in a crystal lattice. Which means that the magnitude of the wavelength have to be few $\mathring{A}$, that is equivalent to have X photons with energies in the range of $(5 \div 25)KeV$. The same treatment of the diffraction theory that was made for the LEED in the previous chapter is still valid for the X-Rays. Also in this case, the Von Laue condition has to be satisfy and also the graphic method of the Ewald sphere is valid. As for LEED, from the spatial distribution of diffracted beam can be deduced the crystal structure, because the diffracted pattern represents the Reciprocal space. In SXRD, besides the information of sample crystal structure, it's possible to get information about the atomic arrangement inside the unit cell, from the measurement of the intensity of the diffracted beam.

3.3.1 Interaction of X-Rays with matter in the Kinematical approximation

X-Rays interact strongly with atoms in solid state matter. It is due to the comparable lenghts between the X-Rays wavelength and the interatomic distances.In particular, the wavelenght λ, i.e. the characteristic length in which the electromagnetic field of the radiation changes, is comparable with the length in which the atomic field is strong. The scattering of X-rays in solid state matter, can be seen as a coherent deflection of the electromagnetic wave field by the strong atomic potential[32]. In general, this phenomenon is described by the dynamics X-Rays scattering theory. This theory is complex because it considers multiple process of scattering[32]. As said previously, for the X-Rays interaction with matter is possible to apply the Kinematical approximation or Born approximation. In this approximation, energy gain or loss and multiple events of scattering can be neglected[27]. In a simplified description[2], the interaction between X-Rays and atoms could be viewed as an excitation of the electrons due to the absorption of X photons. Then, the electrons come back in the ground state with a radiative de-excitation process, i.e. with the emission of a spherical wave with the same wavelength of the incident beam[32]. In the hypothesis that the detector is far away, the spherical wave can be considered as plane wave. This is the far-field approximation[32]. Considering these approximations, Born and far-field valid, the scattered amplitude from a single electron could be written as:

$$A(\vec{k}) \propto e^{i \cdot \vec{k} \cdot \vec{r}} \quad [32]$$

Atoms are in general multi electrons systems. Then, the scattered amplitude from an ensamble of electrons have to be considered. The kinematical approximation simplifies the problem, because it allows to consider these scattered plane waves in a independently way. The scattered amplitude from a multi-electrons system will be simply the sum of all the plane waves, with the correct phase factor[32]. This phase factor is the phase

[2] A very strong semplificate vision of the process. It neglects polarization, inelastic scattering...[32]

difference between the two scattered waves, it represents the difference of the travelled path and is equal to $\vec{Q} \cdot \vec{r}$[32] where $\vec{Q} = \vec{k_f} - \vec{k_i}$ is the momentum exchange. The scattered amplitude from a single electron can be rewritten as:

$$A(\vec{Q}) \propto e^{i \cdot \vec{Q} \cdot \vec{r}} \quad [32]$$

The scattered amplitude from a N multi-electrons system, will be the sum of the the scattered amplitude from each electron, each of which is labeled by the index i. It is equal to:

$$A(\vec{Q}) \propto \sum_i e^{i \cdot \vec{Q} \cdot \vec{r_i}} \quad [32]$$

This equaition could be modified, introducing a δ function that represents the position of the charges in the atom :

$$A(\vec{Q}) \propto \sum_i \int \delta(\vec{r} - \vec{r_i}) e^{i \cdot \vec{Q} \cdot \vec{r_i}} d^3 r \quad [32]$$

Exchanging the order between the integral and the sum, the relation above can be rewritten as:

$$A(\vec{Q}) \propto \int (\sum_i \delta(\vec{r} - \vec{r_i})) e^{i \cdot \vec{Q} \cdot \vec{r_i}} d^3 r \quad [32]$$

The sum of the δ functions is the electron density distribution $\rho(\vec{r})$[32].

$$A(\vec{Q}) \propto \int \rho(\vec{r}) e^{i \cdot \vec{Q} \cdot \vec{r_i}} d^3 r \quad [32]$$

The integral above is the atomic form factor $f(Q)$, it is the Fourier transformation of the electron density of a single atom[32][27]. $f(Q)$ represents the capacity of scatter X-Rays of a particular element[32]. It is, in fact, characteristic of each chemical elements because it depends on their charge distribution. The atomic form factor is a complex number and it depends only by the $\mid \vec{Q} \mid$, because the atoms have spherical symmetry[32]. The phase of $f(Q)$ can't be known. In fact, what is measured is the intensity of the scattered radiation that is proportional only to the absolute square of the scatterd amplitude, i.e. $I(\vec{Q}) = \mid A(\vec{Q}) \mid$.
The next step is consider the crystal structure, starting focalizing the attention on the unitary cell. For the calculation of the scattered intensity of the unitary cell, the position of the single atoms inside the cell have to be taken in account, also with the scattering contribution of each atoms, that is their atomic form factor $f(Q)_j$. Then, what is called the structure factor, is equal to :

$$F(\vec{Q}) = \int_j f_j e^{-M_j} e^{i \vec{r_j} \cdot \vec{Q}} \quad [34]$$

where j represents the label of the atoms inside the unitary cell and their positions are pointed by the vectors $r_j = x_j a_1 + y_j a_2 + z_j a_3$ [3], where x_j, y_j, z_j are the fractional coordinates[34]. f_j, as said before, is the atomic form factor. The factor e^{-M_j} is the Debye-Waller factors that takes accounts for the thermal vibrations[1][34]. The structure factor is the Fourier transform of the electron density for one unit cell of the crystal[27]. The information expressed by this quantity, is the extent of how much the intensity of the scattered waves decreases or increases and it depends on the relative positions of the ions in the unitary cell. The total scattered amplitude from a crystal, since the unit cells in a lattice are identical, is equal to the sum over all cells of their single contribute, which differ one each other only for a phase factor equal to $e^{i\vec{R}\cdot\vec{Q}}$. Where $\vec{Q}$ is the momentum transfer and $\vec{R} = n_1\vec{a_1} + n_2\vec{a_2} + n_3\vec{a_3}$ is the lattice's vector. The total scattered amplitude is then equal to:

$$A_{tot} = A_0 \sum_{n_1,n_2,n_3}^{allunitcells} e^{i\vec{R}\cdot\vec{Q}} \int_j f_j e^{-M_j} e^{i\vec{r_j}\cdot\vec{Q}} \quad [34]$$

Where A_0 contains all pre-factors. The condition to satisfy for having diffraction is always, the constructive interference between the different scattered waves from each primitive cells[1]. Which means, that the phase difference between them have to be the same or an integer multiple of λ. In this case, the phase difference is $e^{i\vec{R}\cdot\vec{Q}}$. The contributes from the unit cells are in phase only when the momentum transfer is equal to a vector of reciprocal lattice i.e. $\vec{Q} = \vec{G}$. The vectors of the reciprocal space are defined as $\vec{G} = h\vec{b_1} + k\vec{b_2} + l\vec{b_3}$, where $\vec{b_1}$ $\vec{b_2}$ $\vec{b_3}$ are the primitive vectors of the reciprocal space and (h,k,l)are the integer indexs. The primitive vectors of the direct lattice and its reciprocal space are defined:

$$\vec{a_i} \cdot \vec{b_j} = 2\pi\delta_{ij} \quad [34][1]$$

So, the phase factor becomes $e^{2\pi i(hn_1+kn_2+ln_3)}$, because both (n_1, n_2, n_3) and (h,k,l)are integer indexs, derives that $e^{i\vec{G}\cdot\vec{R}} = 1$ [4]. If this condition is satisfied, the structure factor becomes:

$$F_{h,k,l} = \int_j f_j e^{-M_j} e^{i\vec{r_j}\cdot\vec{Q}} = \int_j f_j e^{-M_j} e^{2\pi i(hx_j+ky_j+lz_j)} \quad [34]$$

The measured diffracted intensity $I_{h,k,l}$ is proportional to the square of the amplitude, in this case: $I \propto \mid F_{h,k,l} \mid^2$. Then by measuring the intensity from a bulk bragg peak the amplitude of the structure factor can be found. So, from this measurement, information about the position of the atoms in the unitary cell can be obtainted. The Fig.3.1 below,explain the diffraction from a bulk crystal.

[3] a_1, a_2, a_3 are the three primitive vectors that generate the lattice[1].
[4] This is also the definition of Reciprocal Space [1]

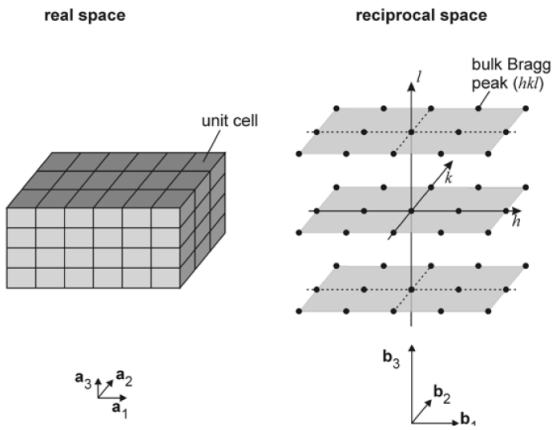

Figure 3.1: Fig. from [34]. In the left part of the image is shown a simplified scheme of a bulk lattice, built from unitary cells. Each unit cell is pointed by a vector $\vec{R} = n_1\vec{a_1} + n_2\vec{a_2} + n_3\vec{a_3}$. Instead, in the right part of the image, is shown the reciprocal space of the crystal, in which is point is identify with a vector $\vec{G} = h\vec{b_1} + k\vec{b_2} + l\vec{b_3}$. Each points of the reciprocal space corrisponds to a Bragg peak when the diffraction from a bulk crystal lattice is measured[34].

3.4 X-Rays Diffraction from a 2D surface

The surface of a Crystal lattice is a 2D system. If a single layer is considered, in particular the topmost, the system becomes a 2-dimensional lattice. In this case, there is no more translational symmetry in the perpendicular direction to the surface. This breaking of the symmetry changes the condition for having diffraction from X-rays . In particular only the parallel component at the surface of the wave vector has to be conserved. For the perpendicular component, none restriction is present. Then, instead of the previous complete condition $\vec{Q} = \vec{G}$, the new condition to satisfy for having diffraction from a surface is:

$$k_{\parallel} - k'_{\parallel} = G_{h,k}[34]$$

Based on the foregoing considerations, the scattered amplitude will be the result of the sum of the scattered waves from the unit cells of the single layer. They are identify by the 2 dimensional vector $\vec{R}_{2D} = n_1\vec{a_1} + n_2\vec{a_2}$. Therefore, the scattered amplitude from a single layer will be:

$$A_{tot} = A_0 \sum_{n_1,n_2}^{allunitcells} e^{i\vec{R_{2D}}\cdot\vec{Q}} \cdot F(\vec{Q})[34]$$

If the condition for having diffraction from a surface is satisfied:

$$A_{tot} = A_0 \sum_{n_1,n_2}^{allunitcells} e^{2\pi i(hn_1+kn_2)} F_{h,k}$$

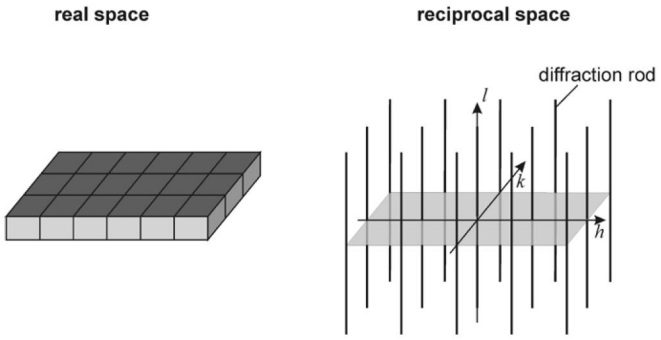

Figure 3.2: Image from [34]. In the left part a scheme of a single layer of the crystal is shown. It is a Two dimensional lattice.In the right part, the reciprocal space is shown. For each couple of values (h,k) a rod is rising in the perpendicular direction. In this case the diffraction will occur for each values along these continuous rods in the reciprocal space.

For having a maximum in scattered amplitude h,k have to assume integer values, otherwise the scattered waves are out of phase and they interfere destructively. While, for the l coefficient no condition have to be satisfied. This means that the diffraction from a single layer occurs along rods in the reciprocal space, instead of points like for a bulk crystal[34]. A scheme is shown in Fig. 3.2.
Consider a single layer is a strong approximation, actually in surface diffraction are involved many of the topmost layers. In this case, the X-ray beam will be absorbed[34] during the propagation and therefore the diffraction will be influenced by this phenomenon. The scattered intensity in this case is equal:

$$A = A_0 \sum_{n_1,n_2} e^{2\pi(hn_1+kn_2)} \sum_{n_3=-\infty}^{0} e^{2\pi il} e^{\alpha n_3} F_{h,k,l}[34]$$

where α is an attenuation factor due to the absoption process. In this equation, the first summation describes as the intensity varies in the layers. Infact the summation is made on n_1, n_2 indexs,thus moving on the ideal single layer. Instead, the second summation is made on n_3, i.e considering a column of unitary cells that starts from the topmost layers and goes deep in the bulk. This term, describes as the scattered amplitude varies along a rods identified by the couples of values (h,k). It takes account of the contribution of identical structure factor from the bulk, linked with a phase factor that takes account of absorption. Evaluating this second summation:

$$F^{bulk}_{h,k,l} = \sum_{n_3=-\infty}^{0} e^{2\pi il} e^{\alpha n_3} F_{h,k,l} = \frac{F_{h,k,l}}{1 - e^{2\pi il} e^{\alpha}}[34]$$

The absorpion has major effect near the Bragg peaks, if it is ignored the previous equa-

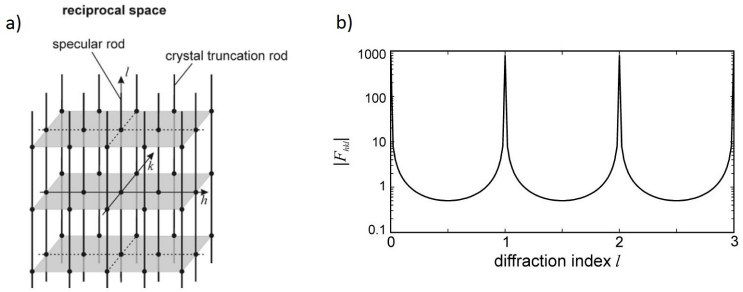

Figure 3.3: Images from [34]. a)Representation of the Reciprocal space of a crystal with a flat surface. The intensity along a rod identify by (h, k) couple of values varies as shown in Fig.b). In this figure the Scattered amplitude along one of these rods is shown. For the characteristic trend of the intensity, this profile is called Crystal Truncation Rod. In particular the intensity becomes huge for integer values of l (positions of Bragg peaks). Instead between them, the intensity became half of the amplitude of a single unit cell, that in this case assumed the unitary value[34].

tions is simplified as:

$$\mid F^{bulk}_{h,k,l} \mid = \mid \frac{F^{u}_{h,k,l}}{2 \sin \pi l} \mid [34]$$

From this equation follows that, the amplitude along the rod is modulated as shown in Fig. 3.3 b. In particular for integer values of l, it rises ideally to infinity, because the denominator goes to zero. Then, at the positions of the bulk Bragg peaks the intensity becames huge. Instead, the presence of a flat surface causes a tail of weak intensity that connects the bulk Bragg peaks[34]. This particular x-ray diffraction pattern is called Crystal Truncation Rods (CTR's)[26][34] and arise from the finite dimension of the crystal in the direction perpendicular at the surface. The previous formula predict and infinite values for the scattered amplitude for integer values of l, this is not correct for a real crystal, in order to obtain a correct value the full dynamical theory should be considered[25]. On the contrary, between two Bragg peaks, the structure factor amplitude assumes very low values. In particular :

$$\frac{I(Braggpoint)}{I(halfvalueofBraggpoint)} = 10^5 [26]$$

These points between the Bragg peaks are the so-called anti-Bragg position[34], the intensity is exactly half of the one that comes from the bulk unit cell, because in this case the scattered amplitude from consecutive layers are in opposite phase then, they interfere destructively. In conclusion,the fact of considering the surface of the crystal, changes the pattern of reciprocal space for which the diffraction occurs. Instead of the points like for bulk diffraction, we a have a crystal truncated rods for each couples of (h, k) values.
Usually, the surface of a crystal is not perfectly flat. Sometimes it has also a different

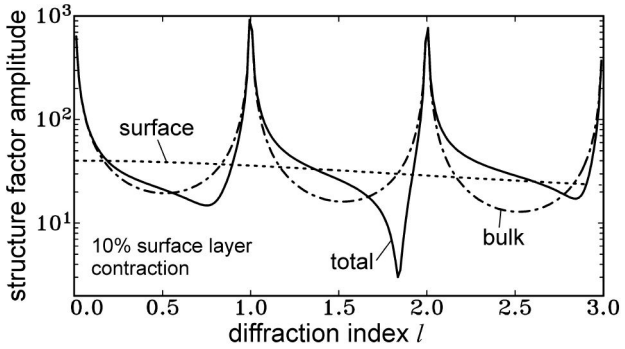

Figure 3.4: Image from [34]. This figure is shown the structure factor of a relaxed surface. In particular the top layer is contracted by a 10%. The surface and the bulk contributes are shown seperately, the total contribute will be their interference sum[34]. This interence is what is measured and is strongly different from the measurement of an ideal case of a bulk terminated surface.

lattice from the bulk one. In this case, it is said that the surface is reconstructed, it means that the size of the surface unitary cell is changing respect to the lattice under. If the surface lattice periodicity is the same of the bulk but changes the interlayer separations normal to the surface, is said that the surface is relaxed. The topmost layers shoul be compressed or extended. These changes of the surface, i.e. a reconstruction, a relaxation or a combination of these phenomena, will change the pattern of diffraction. In particular the total scattered amplitude will show a different trend from that one obtained previously considering a perfect surface.

3.4.1 Technical details

The total scattered amplitude will be a coherent superposition of the bulk and the surface contribution[34].

$$F^{tot}_{h,k,l} = F^{bulk}_{h,k,l} + F^{surf}_{h,k,l} \text{ [34]}$$

Then, if the surface is modified, the total scattered ampitude will show this changing. In particular, as said previously there are two important changing of the surface, the reconstruction and the relaxation. Different patterns occurs depending on whether the surface is reconstructed or not. When the surface is not reconstructed, the unitary cells are the same, therefore the points of the reciprocal space for which will be diffraction are the same shown in Fig. 3.4 a). The difference with the ideal case, will be in the intensity along the CTR. The amplitude along a rod depends strongly by amount of relaxation [34]. An example is shown in Fig.3.4, it is evident in this figure that a relaxation of the topmost layer changes significantly the structure factor profile. On the contrary when the surface is reconstructed, the unitary cell of the surface, will be a multiple of the bulk one. The larger superficial periodicity is called superstructure[17]. In this case, new

crystal truncation rods will appear in the diffraction pattern. In addition to the bulk CTRs for integer value of (h,k) indices, will appear the superficial CTRs at fractional value of (h,k). Their position in the reciprocal space, depend on the periodicity of the reconstruction. They are called superstructure rods or fractional-order rods[34]. These rods contain no bulk contribution, thus at these locations in reciprocal space contain information from the surface only, even though the X-ray beam may deeply penetrate the bulk. Moreover, the amplitude variation along the fractional-order rods depends on the number of layers participating in the reconstruction. Finally, another information about the surface can be gained from this rod profile measurement, the roughness of the surface. The increasing of the surface roughness, cause the decreasing of the amplitude of the rod in the so-called anti-bragg peaks. At some point, these intensity become so weak in intensity that they are not distinguishable from the background signal[34].

Chapter 4

Synchrotron

The synchrotron facilities have become in recent years major research centers for the investigations of condensed and living matter properties. A synchrotron is a powerful source of x-rays, in an energy range $(10 \div 120)$ keV. The characteristic of this so called *synchrotron radiation*, that are completely different from the radiation produces by the common x-rays sources, make synchrotrons unique instruments for the study of science of matter. They are multidisciplinary research centers, that deal with vast fields of research (from Chemistry, Physics, Biology, environmental science etc..). Synchrotron facilities consists in a storage ring in which circulate high speed electrons, nearly of the light speed. This ring is formed by sequences of straight and curved sections. The electron trajectory is bended by a strong magnetic field. Force the electrons to travel along a circular trajectory, means that they are always decelerated by the centripetal force. When a charged particle is accelerated, it emits electromagnetic radiation, and it is the physical phenomenum at the base of the generation of synchrotron radiation. As a result of this irradiation process, the electrons lose their kinetic energy. Therefore, in order to maintain the energy constant along the ring, the electrons are further accelerated by electromagnetic lenses which act in synchronized way. The European Synchrotron Radiation Facility (ESRF), situated in Grenoble(FR), is an excellent research center. It was the first synchrotron of third generation and it is in operation since 1994. Its storage ring measures 844 meters in circumference and it has a storage ring energy of 6 GeV.

4.1 Radiation

In according with the laws of electromagnetism, an accelerated charge emits electromagnetic radiation. The experimental observations show that, if the speed of the charge is low than the speed of light, the particles produce low frequency radiation uniformly in all directions. Instead, if the velocity of the particles approaches to the speed of

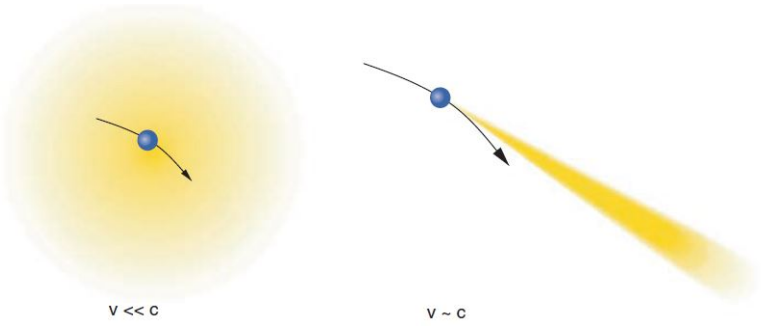

Figure 4.1: Different irradiation process by an accelerated charged particles. The key parameter is the particles velocity: if the velocity of the particles is much smaller than the speed of light, the electromagnetic radiation emitted is isotropic. Otherwise, when the velocity of the particles approaches to the speed of light, the particles emit a collimated radiation along them travelling direction. Image from [35].

light, as happens in a synchrotron, the frequency, the intensity and, most important, the directionality of the emitted radiation are increased (ref. Fig.4.1). Therefore, the synchrotron radiation is a narrow beam of light, emitted in the same direction of the electron motion.

The nearly-relativistic velocity of the electrons circulating in the ring gives to the synchrotron radiation important properties:

- *Brilliance*
  It is defined as the number of incoming photons per second, per unit source area, unit solid angle and unit bandwidth. Brilliance, gives information of the light beam quality, essentially it indicates how the photon flux is distributed in space and angular range. High brilliance, points out a radiation with a narrow and highly parallel beam with high intensity. Synchrotrons have high brilliance, ten orders of magnitude higher than common x-rays laboratory source, for example ESRF produces a beam with a brilliance about 8×10^{20}[ph/s/$mrad^2/mm^2$/0.1% BW]. Since, high brilliance is also the synonym of high intensity, this feature makes synchtron radiation suitable for the study of small amounts of materials or surfaces, because otherwise in these cases, the signal would be not measurable due to low intensity.

- *Divergence*
  Divergence is the opening angle of the beam. Synchrotron emits a very collimate beam, shaped as a narrow cone, thus the synchrotron radiation has low divergence. This feature derives from the relativist velocity of the electrons. The opening angle of the emitted radiation, is inversely proportional to the storage ring energy, namely $\theta \sim (\gamma)^{-1}$, where

$$\gamma \propto E[GeV]$$

For example, for typical storage ring energy range $(1 \div 8GeV)$ the divergence is equal to $(0.5 \div 0.06)$mrad [35].

- *Tunability*
  The frequency of the synchrotron radiation can vary on a continuous range of energies, starting from the infrared to hard X-rays. At the origin of this large spectral width, there are again relativist effects. As a result of the extreme collimation of the emitted radiation, the sample is illuminated only for a very short temporal interval. This narrow temporal pulse corresponds, for the uncertainly principle to a broadband of frequency.

- *Polarization*
  The synchrotron radation is linearly polarized in the plane of the electronic orbit(i.e. the plane of the ring). Depending on the observer positon, above or below the plane, the polariation of light changes. In particular, it is left-circularly polarized if it is observed from above the plane and Right-circularly polarized if it is observed from below. This light feature is fundamental for the study of the magnetic property of materials.

4.2 Architecture

A modern synchrotron facility consists of these fondamental parts (shown in Fig.4.2); the electron source, a linear accelerator, a booster synchrotron, a storage ring and finally, the beamlines or insertion devices. The electrons are emitted in bunch by thermionic effect, from an **electron gun**. They are subsequently accelerated up to about $100KeV$ by a **LINAC**, a linear accelerator. After that, the electrons are injected in the **booster ring**. It is an internal circular ring, with a smaller diameter (about 300 metres). Inside the booster, electrons are further accelerated to reach energies about 6 GeV. Since the path inside the booster is circular, the electron trajectory has to be bended, that is obtained thanks to the use of bending magnets that change their trajectory. The accelerator systems consist in Radio-Frequency cavities, where an oscillating electric field is produced. This oscillation needs to be synchronous with the passage of electrons, in order to obtain the desired effect: if the electrons enter in the RF cavity at the right moment, the slower electrons will receive a boost, instead faster electrons will receive a lower one [35]. This syncronous fenomenum gives the name to the entire structure. From the booster, electrons are periodically injected, when a refill is necessary, into a bigger one ring, the **storage ring**. As said previously, it has a circumference of 844 meters and a pseudo-circular shape trajectory, i.e. a sequence of straight and curved sections. The trajectory of the electrons is maintained circular thank to bending magnets. Along the storage ring are present: quadrupoles and sextupoles, used for focusing the beam, bending magnets and undulators, for the generation of x-rays and RF cavieties, with the task to keep constant the speed of the electrons. Finally, as electrons interact much with the air, to avoid further loss of energy, their entire path must be kept in Ultra High

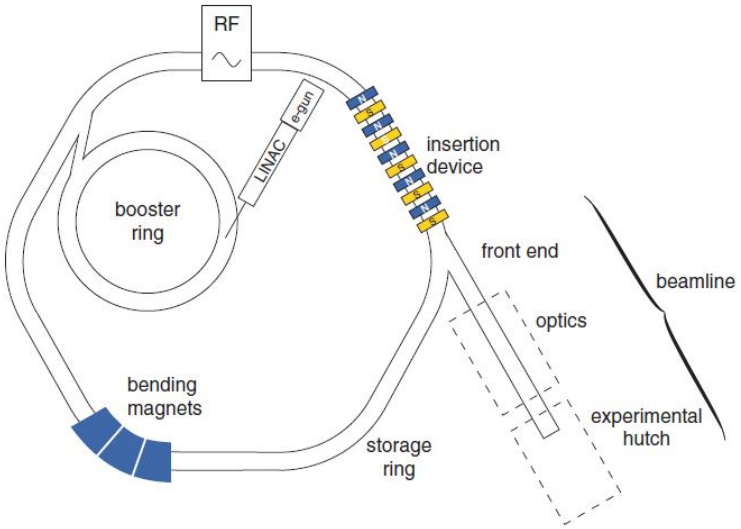

Figure 4.2: Scheme of the most important components of a synchrotron, image from [35].

Vacuum conditions (pressure $< 10^{-9}$ mbar). X-rays are emitted every time that the electronic beam pass from the bending magnets (BMs), ie in the curved sections or in the straight section, by the insertion devices (IDs), subsequently the radiation is directed towards the **beamline**.

Bending magnets and insertion devices Among the different elements present in the storage ring, Bending magnets and Insertion Devices, are those who have the task of producing synchrotron radiation. The radiation emitted from these two devices is significantly different.
Bending magnets are dipole magnets that produce a homogeneous magnetic field along their distance (strenght about 1 Tesla). When the electron beam passes through the bending magnets, the trajectory of the electrons is bent by the force of Lorentz. A change of trajectory is equivalent to a deceleration and therefore a beam of x-rays are emitted tangentially to the plane of the electron beam. This radiation covers a wide and continuous spectrum, but it is not a good quality radiation in terms of focus and brilliance.
Insertion devices are present in third-generation Synchtrons. They are a magnetic structure, made by a complex array of magnets that point alternately up and down, as shown in fig.4.3. They are positioned in the straight sections between BMs and can be classified as wigglers or undulators. The electron beam is forced by this structure to follow an undulating trajectory. The radiation emitted at each consecutive bend interferes with the one emitted from the previously bends. The result is a much more focused and more brilliant beam, than the one produced by bending magnets. In generally, both BM and

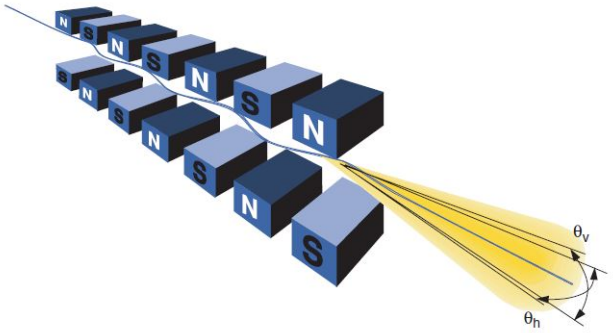

Figure 4.3: Scheme of Insertion device from [35]. The emitted radiation has an angular spread,in horizontal and vertical plane.

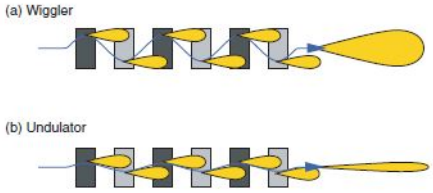

Figure 4.4: Comparison between Wigglers and Undulators. Image from [35].

IDs are used as X-rays source, because not all the experimental techniques used at ESRF require high brightness and high focusing.
The difference between the types of insertion devices,undulators and wigglers, is in the degree of deviation from a straight path in the electron trajectory. This different angular excursion has a fundamental effect in the radiation nature. The wigglers force the beam to execute a larger excursion from the axis, it is larger than the natural opening angle of the radiation. As a consequence, the radiation from each wiggles do not overlap and so the intensity are added. Accordingly, the wiggles provide an high power X-rays beam with a broad spectral range. On the contrary, the undulators force the electron beam to a gentler excursion. This allows the interference of the emitted radiation. Only certain wavelenghts interfere constructively, therefore the undulators spectrum consist of regularly separated narrow bands of radiation, the fundamental frequency and its higher harmonics[35].

Beamline After being emitted by BM and IDs, the radiation is directed towards the beamlines. Many definitions can be attribuited to them; they are the places where experiments take place, but also, the set of fixtures that focus the X-ray radiaion on the sample and record what happens. They are positioned tangentially to the storage ring. In particular, along the axes of the insertion devices and tangentially at bending magnets. The first section of a beamline, is the so called *front end*. It is positioned

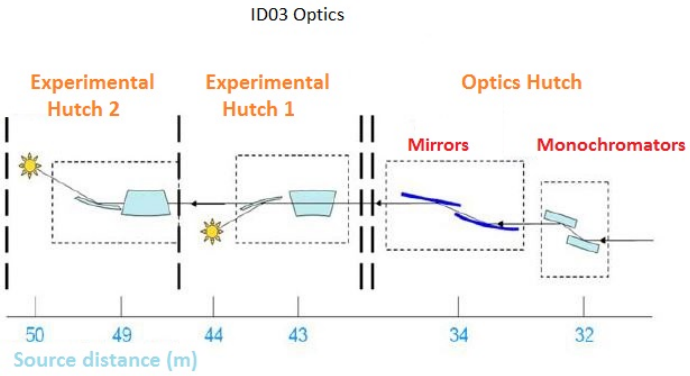

Figure 4.5: A schematic representation of the optical elements at the ID03 beamline. The beam goes from right to left and passes through, the optical hutch before and then, the two experimental huthces.Image from [2].

after the insertion device and has several functions; as isolates the beamline vacuum from the storage ring vacuum or blocking with its closure the X-rays beam, when is required. When the front end is opened, it monitors the beam position and define the angular acceptance with the use of two pairs of slits. Moreover, it filters out, the soft X-rays component of the synchrotron radiation (i.e. with energy below 5 KeV) which, strongly interacts with matter and can damage others components of the beamline. The front end is followed by the optic hutch, where the beam is focused and monochromated. After being modified, the beam enters in the experimental hutch, where depending on the beamlines, it will find a different set equipment. Infact, each beamlines is designed for a specific technique and a specific type of research. Finally, there is a control cabin, where users can drive devices that control the position of samples, regulate the beam and collect data. All by the use of custom software.

4.3 ID03

Every beamline at ESRF is dedicated to a particular technique or topic. $ID03$ is specialized to the in-situ studies of the structure and morphology of surfaces. This beamline, deals with characterization of reactions and dynamics process, that occur on the surface, in real time and real working conditions(i.e. high pressure up to 1bar). Different experimental techniques are available in this beamline, such as Surface X-Ray Diffraction (SXRD), Grazing Incidence Small Angle X-Ray Scattering (GISAXS), Anomalous diffraction and X-Ray Reflectivity (XRR). $ID03$ has three hutches, Fig.4.5, the optic and two experimental hutches ,namely $EH1$ and $EH2$. The beamline is generated by three undulators, which supply a uniform photon flux with an energy range $(6 \div 25)$KeV.

4.3.1 Optics hutches

As said previously, optics hutch is the first hutch after the front end of the beamline. Its task is to modify the beam and make it suitable for the type of experiment that will be performed. All the beam path in the optics hutch is kept in conditions of ultra-high vacuum by the use of pumps(ionic and turbomolecular). In this way, the dispersion of the beam in the air is avoided. The main opticals elements of an optics hutch are: a monochromator, mirrors, slits and filters. As x-rays are strongly absorbed by condensed matter,they are difficult to manage. For this reason, the optical componenents used in an optics hutch are very different from the standard one, used for visible light. As the experiments normally require a well-defined wavelenght of the synchrotron radiation, the first element along the optic path is the *monochromator*. It exploits the diffraction phenomena to separate the different wavelength of the incoming polychromatic light, and select a narrow range of energies. This is normally achieved with a diffraction grating. For hard X-rays, a crystalline solid is employed as monochromator, in $Id03$ is used a monolithic channel cut $Si(111)$ crystal [2]. These crystalline monochromator, must withstand the radiation damage, mainly due to overheating. Thus, they are choosen with a good thermal conductivity and they are cooled by liquid nitrogen. An *attenuator* is placed before the monochromator, its purpose is to filter the incident radiation in order to prevent any damage due to a too intense beam. After the monochromator, a bendable *toroidal mirror* is used to focus the beam at the desired point in the experimental hutch. The surface of this mirrors is concave, with the correct curvature in order to achieve for all incident angles the condition for total external reflection. X-rays have a refractive index slightly below the unit for all condensed matter, and so the only way to obtain their reflection from a surface, is incidence at grazing angles. In particular, at angles minor than the critical one, and exploit thus, the phenomenon of total external reflection. The toroidal mirrors is enable to focus the beam, both in horizontal and vertically directions, with a characteristic focal size of $(40 \times 30)(\mu m)^2$. Finally, along all the beamline path, *slits* are present with the task of regulate the vertical and horizontal divergence of the incoming beam. For safety reasons each hutch is separated from the other by shutters,namely rapidly closing valve, aimed to blocking the beam, when necessary.

4.3.2 Experimental hutch 1

As shown in Fig.4.5, following the optics hutch, is located the Experimental hutch 1. This first laboratory is dedicated on surface characterization, especially in catalysis studies. In the experimental hutch 1 are present; optical instrument to direct the beam onto the sample, different types of reactors, each one suitable for a different experiments and finally, devices aimed to collecting the signal coming from the sample. As regards optical elements, even here there are present mirrors, slits, shutters and attenuators. For

what concerns the focusing system, both vertical and horizontal focusing KB [1] mirrors are situated along the beam path. Being $Id03$ a beamline dedicated to the study of surfaces, various in-house equipments are available for this purpose. In particular, are available, batch reactors equipped with a gas line system, an electrochemical cell and a flow reactor [2], which allows the characterization of catalytic processes. All the reactors, are equipped with the necessary experimental set for the cleaning procedure of surfaces as, an UHV set equipment (pumps and gauges), Ion Sputter gun and a sample holders by which is possible heat up the sample, thus performing the annealing process.
$EH1$ is equipped with a *vertical* diffractometer, proper for surfaces with a horizontal geometry. This six-circle diffractometer, is a robust diffractometer designed to host big and heavy setups. As the name suggests, this type of diffractometer has six degrees of freedom, namely six angles can be defined. The diffractometer has an arm, on which is mounted a detector. The sample is positioned on a six legs support, the hexapode. It was concerned for setting, with high precision the position of the sample. The hexapode rests on the basis of the diffractometer and it can endure a maximm weight of 200 Kg. In this configuration, the sample surface is horizontal and is positioned in the center of rotation axis of the hexapode. During the experiment, three of the six angles are fixed: μ ϕ and χ. They are defined at the beginning of the beamtime, for the alignment of the beam. Instead, the others angles are changed thanks to the in house software *spec*, controlled by the users from the control room. In paticular, θ turns the sample around its surface normal, δ moves the detector in the surface plane and γ moves it perpendicularly at the surface plane. Regarding the x-ray detector, $ID03$ uses a photon-counting pixel detector, in particular a $2D$ MAXIPIX with an area of $512x512$ pixels. This detector records, spatially resolved information from a region in space, in a single shot. MAXIPIX detectors were developed by ESRF for the beamlines. This device is inspired on the previous model, the MEDIPIX [13] developed by CERN. The main features of the maxipix are, high spatial resolution, in a range $50 \div 100\mu m$ (pixels dimension) and high frame rate, up to 1.4 KHz with readout time very short($290\mu s$).

4.3.3 Experimental hutch 2

The second experimental hutch is situated after EH 1. In order to extend the beam until the experimental hutch 2, is used a fly tube that keeps the path in UHV condition. This experimental station, employs a *horizontal* geometry z-axis diffractometer, specialized to UHV studies, in fact it is combined with a UHV chamber. This chamber, also allows in-situ surface preparation. For this purpose, it is equipped with a ion sputtering for surface cleaning, a ion gun and a Cylindrical Mirror Analyser(CMA) for the Auger Electron Spectroscopy. The UHV chamber is also equipped with a mass spectrometers or Residual Gas Analyzer (RGA), for the real-time monitoring of the chemical composition

[1] KB stand for Kirkpatrick-Baez, the inventors of the setup. This system is constituted by mirrors and motors. Mirrors are made of silica and they are controlled by motors, which rotate and translate the mirror.

[2] see paragraph 4.4

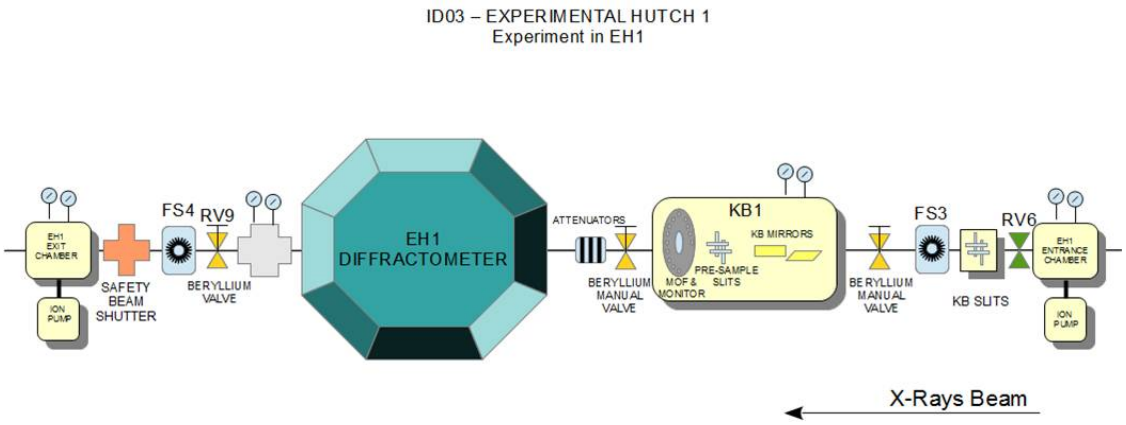

Figure 4.6: Setup of the first experimental hutch in *ID*03.

of the gas in the UHV chamber.
Moreover, the UHV chamber lets the simultaneous deposit of three samples inside the UHV setup, thanks to the load-lock system. This system is constituted of five basic components including a sample staging chamber, gate valve, sample transporter, quick-access door and an observation window. Samples are mounted on magnetic sample holders, and are then loaded, thanks to a magnetically coupled transporter through to a 'quick access' door. Loading procedures, can be monitored through the viewport positioned directly above the access door. Then, this chamber is evacuated to the vacuum level and when to the desired pressure is reaches, the chamber load-lock valve is opened and the sample is transferred into the main chamber. This solution reduces the time required for the exchange between samples, because allows a simple and fast loading or unloading process, that occurs without breaking the main system vacuum.

4.4 Flow reactor: Ufo chamber

The flow reactor is an instrument particularly suitable for studying catalysis reactions. It allows an in situ characterization of the catalyst surface by synchrotron radiation. What makes this setup fitted for this kind of studies at synchrotron, is its features of being simultaneously a flow reactor and a UHV chamber, in which doing the sample preparation. The main advantage of the 'Ufo chamber'[3], is the transferring among the two configurations, UHV chamber and Flow reactor, without exposing the set up to air. Otherwise, the sample has to be tranferred between two different the setup and this, during the experiment time requires a realignment of the sample respect to the beam, for each movement. This leads to a waste of time, that is valuable during the beamtime. Moreover, the advantage of the flow reactor respect to the batch mode,is that the gas

[3]so called because of the shape.

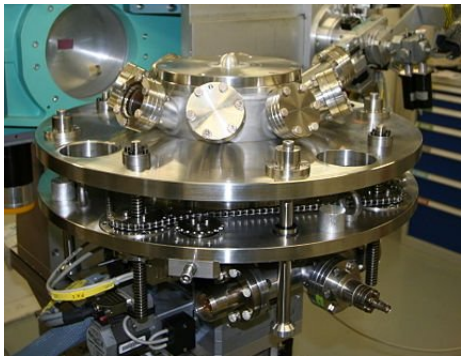

Figure 4.7: Flow Setup

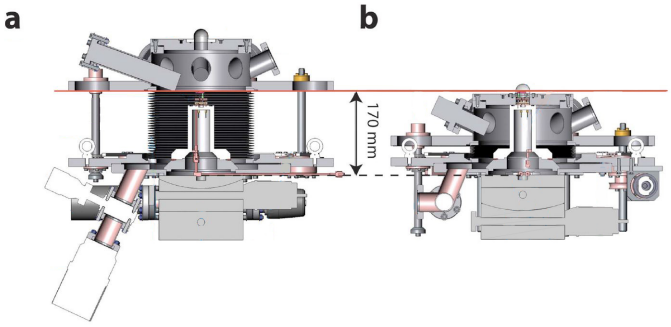

Figure 4.8: a)lateral section view of the setup in UHV configuration. b)lateral section view of the setup in reactor configuration. Image from [33].

composition could keep constant during the measurements inside the chamber. This Flow reactor, shown in fig.4.7, was developed by a collaboration between the beamline staff at ID03 and the interface physics group at Leiden university. It was designed to be suitable for the six-circle diffractometer and for obtained a quick sample exchange[33].

4.4.1 Chamber design

The flow chamber consists of two steel plates connected by a bellow. The lower plate holds the sample holder, the quadrupole mass spectrometer and the turbopump. Instead, the top plate holds the ion gun and the evaporator[33]. The top plate can be translated vertically through the extension of the bellow and it is this shift that allows to the instrument to have two compartments. When the bellow is completely extended, the ultra high vacuum preparation part is present on the contrary the reactor part is present when the bellow is completely compressed. This is obtained by a chain drive mechanism. When the setup is open, in ultra high vacuum configuration the preparation of the sample can be done: cycles of sputtering, annealing and also depositing of metal on the sample surface. Otherwise, when the setup is closed, the sample is confined in a small volume

defined by the top flange and the beryllium dome. Beryllium is a low Z-material, it is transparent for X-rays and this is the reason for its employ.The reactor wall are cooled by water flow in order to prevent unwanted reactions. The instrument also provides, the introduction of a gas mixture in the reactor part.In particular, gas are mixed in a gas system and they are transported to and from the reactor thanks to capillaries that appear from the sample holder. The gas analysis is made with the opening of the leak valve positioned in the exhaust pipe. This valve connects the pipe with the ultra high vacuum compartments where is present the mass spectrometer. The flow setup allows to determine the surface structure and morphology under reaction conditions because the gas pressure reach the near ambient condition in the reactor compartment. Moreover,the gas composition is determined by mass spectrometer in real time. So, a correlation between this two measurements is possible.

4.5 Sample holder

Different sample holders are avaible at $ID03$. They share a common design for being installed in the different preparation chamber or inside the flow reactor, but according to the type of experiment, different materials are used for its components. For example, for experiments in the flow reacotr, the sample holder have to be made by materials that are not catalitically active, as Cu or Pt. The scheme of the sample holder is shown in Fig.4.9. The sample is in contact with a boraelectric heater made of an graphite element covered by boron nitride, which makes it chemically inert at CO O_2 H_2(common gases used in the flow reactor). This structure is used to heat the sample (up to 950K) and it is connected, both mechanically and electrically to the plates below through two Tungsten rods. The sample is fixed to the boraelectric heated by a clip, the available ones are made of tantalium or molybdenum. The clip chosen for the experiment is Tantalium, because it is hard to oxidize. It became oxidized at high temperature, so the sample can be heated untill 950K[33]. The temperature of the sample is measured by a thermocoupled, a K-type for the UHV chamber and a type C, made of Tungsten and Rhenium, for the flow reactor, pressed against the sample by two clips mounted on the heater[33].

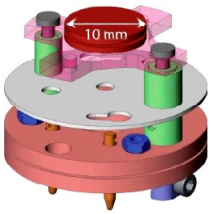

Figure 4.9: Image taken from ref.[33], shows the scheme of the sample holder: the red part is the sample and the pink part is the boraelectric heater. The gray part in contact with the heater are the two Tungsten rods. Below aheat shield, guarantees no heat dispersion.

Chapter 5

Sample preparation

Surface X-ray Diffraction experiments need an atomically flat crystal surface. The only surface defects should be, large atomic terraces having average width of several hundred of nanometers, caused by the 0.05 deg miscut angle of the crystal. Moreover, the chemical composition at surface, must not contain common silver contaminants, as carbon , sulfur, chlorine and tellurium[18]. These two requirements, atomic smoothness and cleanliness of the surface, need to be fulfilled in order to prepare a well-ordered crystallographic surface, which can be investigated using SXRD.
The sample used in the experiment is an hat-shaped disk of (111) oriented single silver crystal, with a size of 10 mm in diameter (8 mm the top plane) and thickness of 2.5 mm. Before the experiments, the sample was polished by an external company. The disk was assembled on the sample holder Fig.5.1, transported in EH1 and inserted in the UHV chamber by using the laod-lock system. The UHV chamber is equipped with a scroll pump and a turbomolecular pump, connected in series. The assembly sequence is: UHV chamber, turbomolecolar pump, scroll pump, atmosphere. The scroll pump is also connected to the UHV chamber with a bypass to create an initial vacuum. It is turned

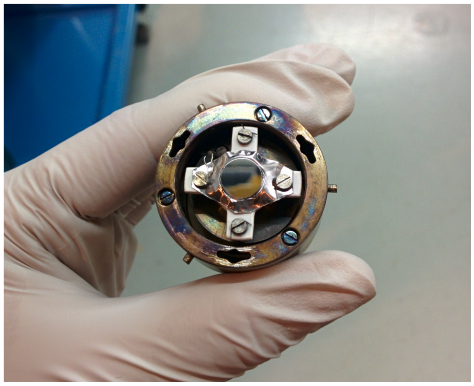

Figure 5.1: Photo of the Silver sample assembled on the sample holder.

on before the turbomolecular pump, in order to decrease the chamber pressure until 10^{-2} mbar. The pressure inside the chamber is monitored by capacitance manometers, Pirani gauge and the ionisation gauge.
The UHV chamber is also equipped with an electron gun and a Cylindrical Mirror Analyzer. Several Auger electron Spectra were recorded, alternated with cycles of sputtering and annealing. For the cleaning procedure, Argon ions were used for the bombardment of the crystal surface. The pressure of the gas in chamber was $pAr = 3 \times 10^{-5}$ mbar and the Kinetic Energy of argon ions set to 0.65 KeV. After every sputtering, the sample was heated by the boraelectric heater in order to remove embedded Ar ions. The temperature of the sample reached approximately 600K and was kept for 15 minutes. The sample temperature was monitored by thermocouple.
Afterwards,the sample was disassembled from the UHV chamber in EH 2, exposed in atmosphere and transported to the Omicron Laboratory[1], where it was inserted in another UHV chamber equipped with an ion gun and a LEED camera. LEED measurements were carried out, followed by cycles of sputtering and annealing. This procedure was repeated until a good degree of crystallographic order was shown in the LEED pattern.

5.1 AES measurements

In order to check the surface cleanliness of the Ag(111) surface, some Auger Electron Spectroscopy measurements were executed. The energy of the primary electron beam was set to 2 KeV. The Auger electrons emitted by the surface were detected by the Cylindrical Mirror Analyzer, and the measurement was then differentiated. The first derivative spectrum is shown in Fig.5.2.a). The AES spectrum revealed the presence of contaminants on the surface. Generally, the surface of crystal samples of pure Silver, may contain Sulfur, Chlorine, Carbon and Oxygen impurities [18], and their main peaks, in the energy range of the recorded spectra ($50 \div 700$eV), are respectively, 153eV, 184eV, 275eV and 510eV [8]. The spectrum showed the presence of two contaminants: the Sulfur, whose peak is at 155 eV and carbon whose peak is at 269 eV. From the reference spectra of carbon and silver, we desume that both have a main peak near this energy. The carbon have a main peak at 275eV (KLL Auger transition)and silver at 267eV (MNN Auger transition)ref.[8]. Therefore, the measured peak at 269eV, could be the overlap of the contributions of this two peaks. In an AES spectrum the measurement of the peak to peak height is proportional to the intensity of a particular Auger transition. In this spectrum the peak to peak height at 269eV is visible higher than the one at 300 eV. From the Ag reference spectra[8], can be observed that the peak to peak height at 300 eV is almost double of the one at 267 eV. That means we have a contribution in this energy range from the carbon peak. Afterwards, many cycles of sputtering and annealing were done. In Fig.5.2 b) is shown the spectrum after the cleaning procedure. The peak of the Sulfur at 155eV has disappeared and the one at 264eV has reduced its peak to peak height by about the sixty percent. But the spectrum was not yet satisfactory, because of

[1] A support laboratory of ID03

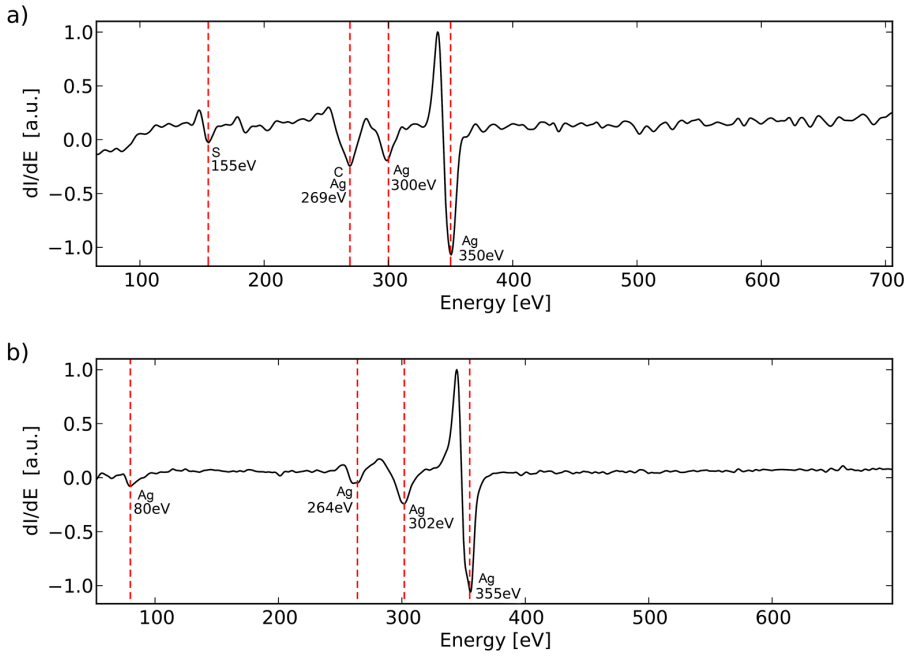

Figure 5.2: First derivative spectra of the Ag(111)surface. Step size 0.5 eV. Each spectrum is normalized respect to the maximum intensity value of its direct spectrum (at $\approx$ 345 eV), then they are derived and finally smoothed with Savitzky-Golay filter. a)AES spectrum recorded before cleaning. The surface is contamined by sulfur and carbon b) AES spectrum recorded after many cycles of sputtering and annealing, the sulfur peak disappears.

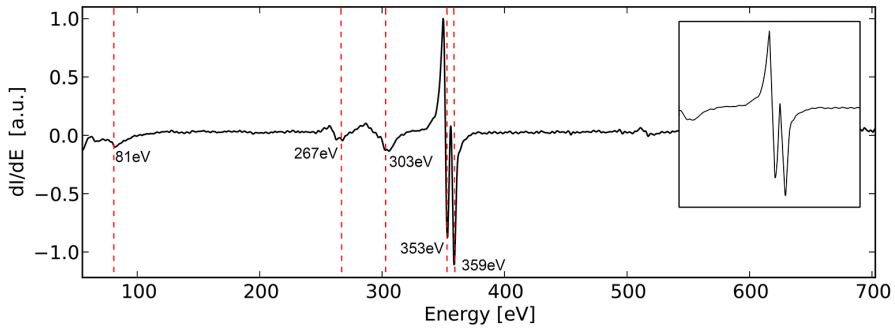

Figure 5.3: First derivative spectra of the Ag(111) surface. Step size 0.25 eV. Final AES spectrum, acquired after prolonged cycles of sample sputtering and annealing. Insert: enlargement of the characteristic 'double peak' of silver.

the absence of some of the silver main peaks. For this reason, further prolonged cycles

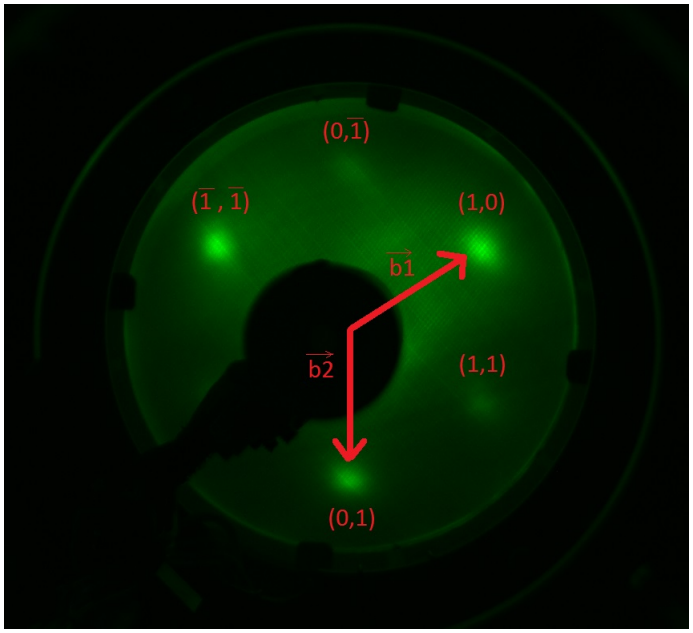

Figure 5.4: LEED pattern of the Ag(111) surface. The dark part in the center of the pattern is the shadow of the electron gun. It is a consequence of the geometry of the experimental set: electrons are generated by the electron gun, they hit the sample surface and the back-scattered electrons hit the fluorescent screen, that is positioned behind the electron source. The pattern is registred by the video camera, arranged after the UHV view port.

of sputtering and annealing were made. Finally, the spectrum was acquired Fig.5.3. In this spectrum, all of the typical peaks of the Silver are present: 81 eV, 267 eV, 303 eV and the double peak at 352 eV and 359 eV. The recorded spectrum corresponds to the reference one.

5.2 LEED measurements

LEED measurements give information about the crystallographic structure of the crystal in first few surface layers. Before the experiment, some LEED measurements were done. The energy of the electrons was set at 140 eV. The low energy of electron beam is suitable for surface studies, since the primary electrons penetrate into the materials for only few Angstroms. The LEED pattern is shown in Fig. 5.4. The pattern is an hexagonal 2D lattice, it is clearly visible that three spots are brighter than the other three. LEED pattern has three fold symmetry, that reflects the symmetry of the FCC 111 surface. FCC crystal lattice, along the (111) direction, consists of layers of hexagonal lattice, that stacked to each other, shifted by one third of the lattice constant. As we can observe in

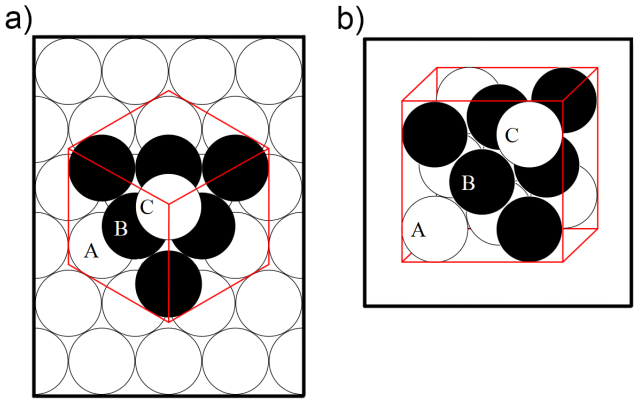

Figure 5.5: Silver crystal lattice from different point of view : a)top view; b)side view. Image from ref.[15]. Three layers, labeled by the letters A,B,C are stacking in sequence ABCABC. The periodicity is thus three times the distance between the planes. From a), it's clearly that the symmetry is three-fold.

Fig.5.5, the Ag(111)surface has a three-fold symmetry and this causes the difference in energy of the peaks. In conclusion, the LEED pattern is not showing a perfect crystal, because the peaks are not very bright in comparison to the backgroung.

5.3 Final preparation

After the cleaning procedures and the LEED and AES measurements, the sample was assembled on another sample holder, suited for the flow reactor. Before the settlement on the reactor, the sample was cleaned by Acetone, in order to remove organic compounds from the surface. Also the other components of the sample holder, like screws and the sample clip were cleaned by an ultrasonic bath of Acetone and Ethanole.

Chapter 6

Oxidation of the Ag(111) surface: Data analysis

6.1 Ag(111): Clean surface

The sample mounted in the flow reactor was further cleaned, using the procedure described before. The set of CTRs of the clean sample in vacuum conditions was recorded in order to check the quality of the cleaned surface. The recorded data were used as a reference for the later measurements, during which, the growth of surface oxides was observed.
The reported graphs, show the plot of the structure factor as a function of the Miller's index L, in reciprocal lattice unit. The structure factor was obtained by using BINoculars software, developed by ID03 team[28]. The software is used for the reduction and the integration of recorded unrefined data by using the 2D detector. In particular, it calculates for each pixel the corresponding position in reciprocal space(hkl) and reduces the data collected by making the average of the intensities of pixels from different images, taken at the same (hkl) position.
As shown in the Fig. 6.1, 6.2 and 6.3 the periodicity of the Bragg's peaks is every three values of L, therefore $\Delta L = 3$. This periodicity reflects the FCC crystal structure of the Silver crystal. A FCC crystal in (111) direction, is composed of hexagonal lattice layers shifted to each other by one third of the lattice constant (ABCABC stacking sequence). Therefore, the crystal in the (111) direction (z direction in the experiment) has a periodicity equals to three times the distance between the layers and this value corresponds to $3 \times 2.36\mathring{A}$.

An X-ray Reflectivity or $00L$ CTR, was measured later, Fig.6.3. In the measures of X-Ray Reflectivity the angle of incidence and angle of outgoing are equal. Then, being also the scattering elastic, the momentum exchange in the plane of the surface is equal to zero $\Delta\bar{k}\parallel = 0$ and as a consequence we are moving along the $(0,0)$ rod. Instead the momentum exchange perpendicular to the plane is proportional to the sine of the

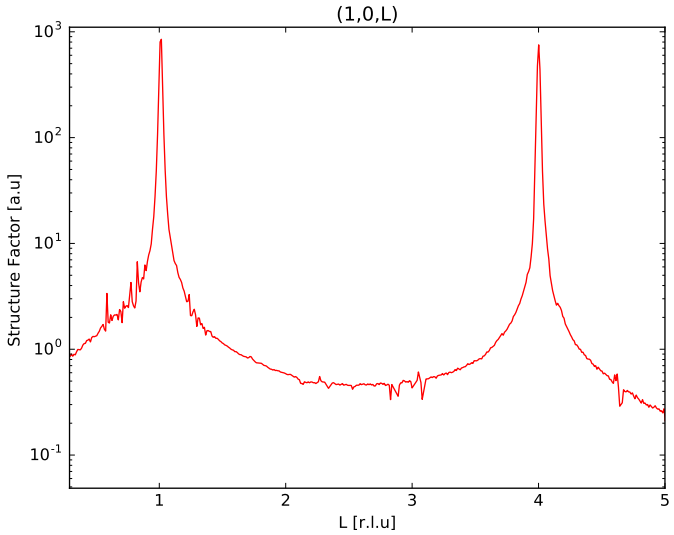

Figure 6.1: Integrated CTR measured in $(h, k) = (1, 0)$ of the clean $Ag(111)$ surface. The periodicity of the Bragg's peaks is three times the Miller's Index L. The signal between the Bragg's peaks produces information about the surface. Rods are plotted using a logarithmic scale of values.

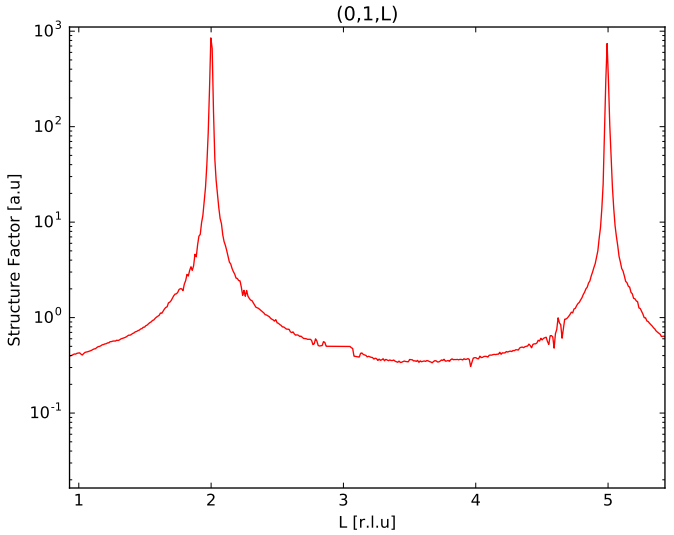

Figure 6.2: Integrated CTR measured in $(h, k) = (0, 1)$ of the clean $Ag(111)$ surface. If we made a comparison with the previous CTR, we can observe that the periodicity of the Bragg's peaks is always the same, but we have the peaks for others values of L.

incidence angle. Curves of reflectivity are measures of intensity as a function of incidence angle, in specular geometry. For the phenomenon of total reflection, if the angle of incidence is less than the critical one, the radiation will be totally reflected. For this reason the real reflectivity curve corresponds to the beginning of the (0,0,L) rod, also called the *specular rod*.
To obtain a XRR measure, the sample and the detector have to move at the same time. The sample must be rotated in order to change the incidence angle. Therefore the angle μ, between the sample and the beam must change. The detector, in order to guarantee the reflection geometry, must follow this changing, varying the γ angle. The detector therefore, measures an intensity as a function of the angle of incidence of the X-rays(μ). In order to plot the structure function of the $(0, 0)$ rod as a function of L values, these values have to be calculated using the Bragg's law:

$$n\lambda = 2d\sin(\mu)$$

The wavelenght is $0.52\mathring{A}$, calculated from the energy of the beam $\lambda = (hc)/E$. The distance between the planes is calculted from the constant lattice, that for the Silver crystal is equal to $a = 4.079\mathring{A}$. The lattice is cubic, therefore the distance between two planes is :

$$d_{(h,k,l)} = a/(\sqrt{h^2 + k^2 + l^2})$$

The direction is the (111), and then $d = a/\sqrt{3}$. Finally I found n, that is the L Miller's index, function of μ.

$$L = (2d/\lambda)\sin(\mu)$$

From the intensity, the structure factor was extracted by using BINoculars and Fitaid. The structure factor as a function of L is plotted in Fig.6.3. This particular rod, gives information about the order of the layers in z-direction (i.e. perpendicular to the surface), because the momentum exchange in plane is equal to zero and so the information given by this measure is related to the out of plane structures. In this case the XRR shows a smooth profile of the curve that allowed us to say that the surface was very well-ordered.
Finally, in Fig.6.4 is shown a 3D model of the reciprocal space of the Silver lattice. The 3D model shows the profile of the measured rods. In Fig.6.5 is shown another way to measure the diffraction peaks and the CTRs, a HK map of the reciprocal space. This kind of measurement is obtained with a scan of the reciprocal space at a fixed value of L, with the 2D detector. BINoculars, then integrates the detector snapshots and in this way it reconstructs the reciprocal space. The scanning of the map was done for L=0.3, therefore it is as if we had cut the CTRs of the Ag(111) surface.

6.2 Oxidation: p (4×4) reconstruction

After the study of the clean surface we started with the oxidation process. A first study was made on the growth of an oxide layer which has a structure of p-(4×4). During

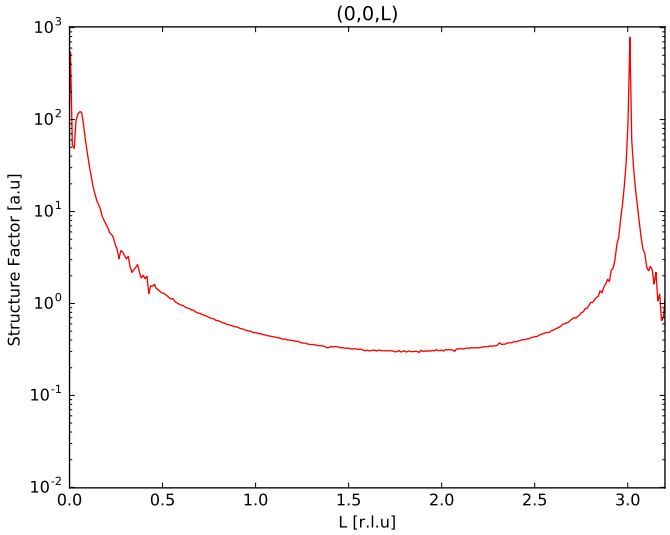

Figure 6.3: Integrated XRR or specular rod. The surface is smooth and clean, because also the beginning of the rod profile is smooth.

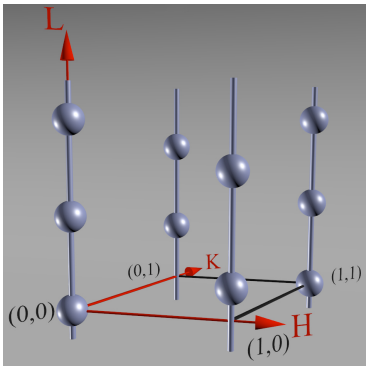

Figure 6.4: 3D model of the reciprocal space of a FCC (111) surface: four crystal truncation rods are shown, three of which were measured during the experiment. The balls represent the Bragg's peaks and the rods that link them are the diffracted intensity that comes from the surface. If I slice the $3D$ space with a plane at different integer values of L, parallel to HK plane, I will see the characteristic hexagonal pattern, similar to LEED pattern showed in Fig.5.4.

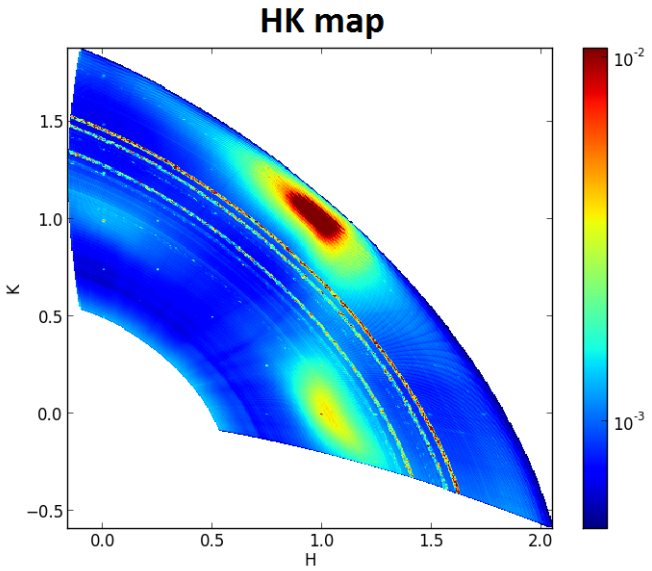

Figure 6.5: HK map of the reciprocal space, acquired for L=0.3. In this map are present sections of the CTRs of the Ag (111) lattice at positions: $(1,0)$,$(0,1)$ and $(1,1)$. note: the rings in the map are due to the scattering of the beryllium dome.

such investigation, the oxygen pressure and the temperature of the sample were modified, in order to establish the temperature and pressures interval for which the structure appears. The oxygen pressure was controlled by SPEC software, the data aquisition software of the beamline. Instead, the sample was heated by setting, from the control room, the current passing in the graphite heating element of the boraelectric heater. The temperature of the sample was monitored by thermocouple.
For this first measurement, the pressure of oxygen was set to 0.4 mbar and the temperature of the sample was set to 423K. In these conditions, the formation of the $p(4 \times 4)$ reconstruction was observed and recorded by several timescan. A timescan is a measurement of the intensity changes in time, acquired with the detector in a fixed position. In this way, a monitoring of the peak at small angles and in a specific position, is done. In Fig.6.6 is shown a timescan, the chosen position to see the diffracted intensity is $(h,k,l) = (0.5, 0.5, 0.3)$, one of the points of the set of diffraction peaks from $p(4 \times 4)$ reconstruction. Diffraction spots from a p-(4×4) reconstruction are observed in one-fourth of the position of the Bragg peak of bulk, because an enlargement of the structure in the direct lattice corresponds to a reduction of the same amount in the reciprocal space.
From the timescan measurement, the formation of the p-(4×4) reconstruction at these conditions, can be demonstrated. But the presence of oscillations in the intensity, means changes on the surface, therefore this reconstruction is not stable. After a further increase of the oxygen pressure, was observed a continuosly decreasing of the intensity for this peak. This is coherent with the previous studies [9]: when the Ag(111) surface is exposed to a high oxygen dose, this oxygen-induced species disappears. Therefore, the

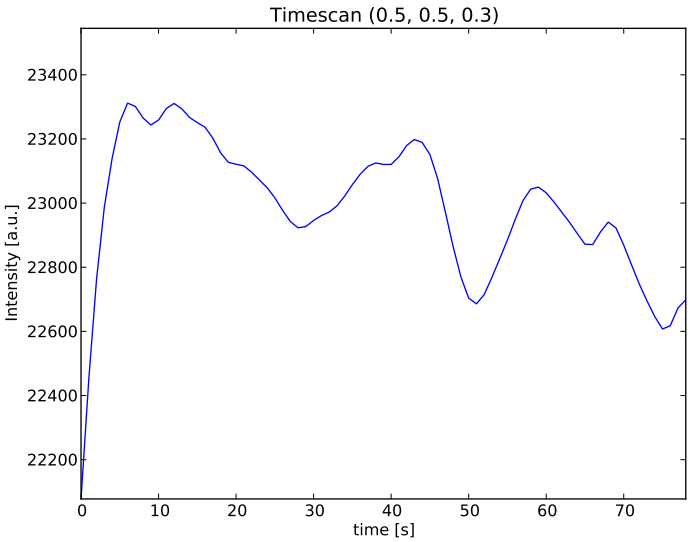

Figure 6.6: Timescan in the position $(h, k, l) = (0.5, 0.5, 0.3)$. This is the position of the peak of the p-(4×4) reconstruction. The peak appears in these conditions, but its intensity oscillates in time. This means, instability, probably because there were some kinetics processes on the surface.

detector was moved in other positions, looking for other oxygen-induced reconstruction on the surface.

6.3 Oxidation: p (7×7) reconstruction

From past studies, it is known that the O-Ag-O trilayer surface oxide and a thick layer of silver oxide Ag_2O, exhibit the same honeycomb structure on the hexagon placement of the Ag(111)surface, this system results in a p-(7×7) coincidence structure[23]. Therefore, to observe the growth of these structures, surface oxide or bulk oxide, the detector was moved in position (h,k)=$(0, 0.86)$ in reciprocal space, which matches with one of the reflections compatible with the p-(7×7) reconstruction. A peak of diffraction was observed, therefore an oxide is formed and in order to know something more about, an L scan was carried out. The CTR is shown in fig. 6.7. The peak in the position $(h, k, l) = (0, 0.86, 0.87)$ is narrow enough, to be able to hypotize that the reconstruction on the surface is thick. The width of the peak gives information about the thickness; the higher is the number of layers, the higher is the number of light waves that interfere constructively and so the peak becomes narrower. For this reason, we supposed that the reconstruction was not a surface oxide, but a bulk oxide. When the Silver becomes Silver Oxide, its FCC lattice undergo to an expansion of the $15,5\%$, due to the presence

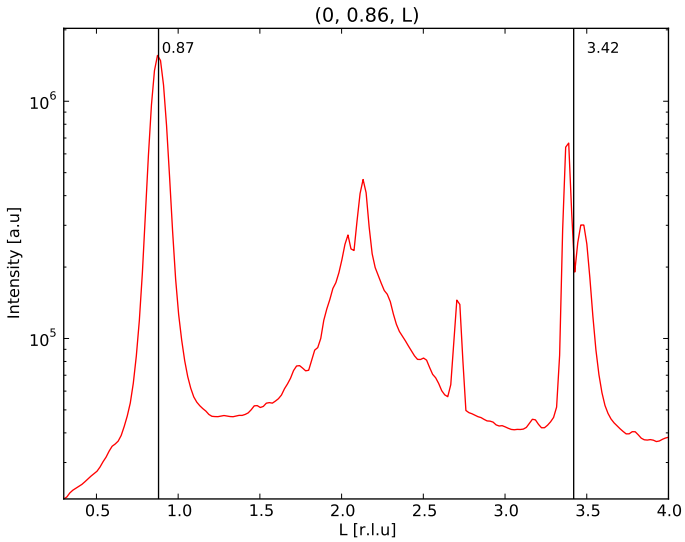

Figure 6.7: Integrated CTR measured in $(h, k) = (0, 0.86)$. The marked peaks are characteristic of the bulk oxide.

of two oxygen atoms arranged along the diagonal of the cube, in a shifted position of one quarter relative to the tetrahedral sites[1]. This expansion in the direct lattice, corresponds to a reduction in reciprocal space. So, the second peak should be to at a distance from the first equal to $\Delta L = 0.85 \times 3 = 2.55$, this is coherent with the position of the second peak at L equal to 3.42. This is a further confirmation that the reconstruction is a bulk oxide. The peak of intensity in the middle, comes from the closeness of the Bragg's peak of the Ag(111) surface at position (h,k,l)=$(0, 1, 2)$.

Comparing the CTRs of the clean surface at $(h, k) = (0, 1)$ in Fig.6.2 with the one of the bulk oxide at $(h, k) = (0, 0.86)$ Fig.6.7, it is possible to recognize a different stacking sequence of the Ag planes, from the 'ABC' types of the Ag(111). In the CTR of clean surface the bragg's peaks are at $L = 2$ and $L = 5$, instead in the bulk oxide are at $L = 0.87$ and $L = 0.87 + \Delta L = 3.42$. For a 'correct' stacking, the peaks of the bulk oxide should be shifted, as in the $(0, 1)$ CTR of the Ag(111). This means that, the bulk oxide has an epitaxial growth with an 'inverted' orientation ('CBA' stacking sequence). This is the Stranski–Krastanov like growth, already observed in the past study[23].
After observing the formation of bulk oxide, the next step was to investigate its stability by changing the enviroment conditions. The previous measure demonstrates the formation of bulk oxide at room temperature, 0.4 mbar of oxygen and with the beam attenuator set to 0. Then, we made a measure at the same pressure of oxygen but the sample was heated.

[1] See Cuprite structure in introduction.

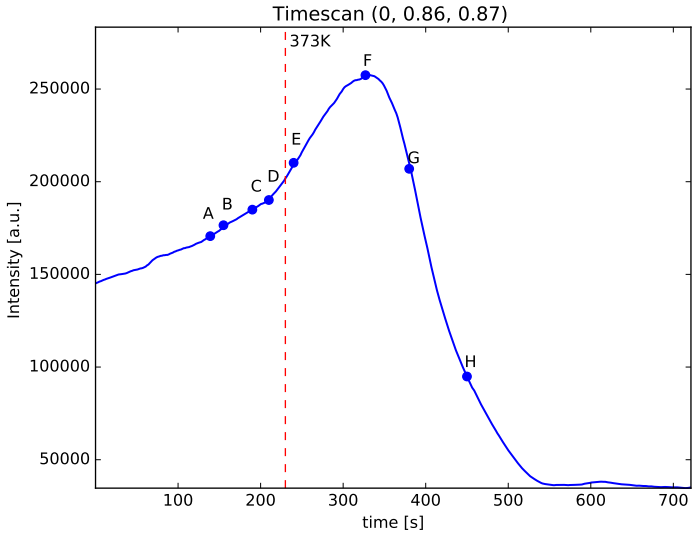

Figure 6.8: Timescan in the $(0, 0.87, 0.86)$ position. The sample was seated in the coordinates :$(x, y, z) = (-0.001, 1.4, 0.0487)$. During this measure, the Oxygen flow was set to zero and the temperature was changed starting from $323K$ up to $493K$. Each point labeled by a letter, corresponds to an image in Fig. 6.9 recoderded by the detector.

6.3.1 Stacking fault

The measure shown in fig. 6.8 is a timescan acquired after the previous oxidation. During this acquisition the oxygen flux was closed and the only parameter that was changed was the temperature. At the beginning of the measure, the sample was heated up to $323K$. Then, the temperature was increased until $373K$ in 230 seconds. At the end of the measure the sample temperature reached $493K$. From this timescan we can observe that the peak of the oxide disappears at the end of the measure, that means it is not stable at high temperatures. In Fig. 6.9 is shown a sequence of images acquired in real time during the timescan measurement. Each image, is taken in different times, indicated in the timescan by letters. During the increasing of the temperature, a new peak in the right of the image appears and becomes more intense as the time goes on. At the end, only the new peak survives. The appearance of a new peak indicates the presence of a new structure on the surface. From the images we supposed the position of this new peak at $(h, k, l) = (0, 1, 1)$. So, a CTR along the direction $(0, 1, L)$ was carried out. The integrated CTR shown in Fig.6.10. If we make a comparison between the CTR taken before and after the oxidation, respectively Fig.6.2 and Fig. 6.10, we see two new peaks rising at position $L = 1$ and $L = 4$. The hypothesis is that with the increasing of the temperature the oxygen atoms start to desorb from bulk oxide. After the desorption, the structure tries to rearrange on the metallic surface in order to minimize its energy. But, as said previously, the bulk oxide grows as 'inverted stacking'

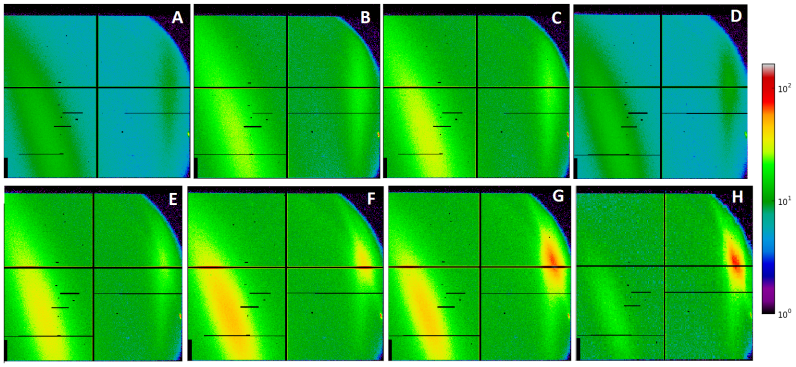

Figure 6.9: Sequence in time of images taken during the previous timescan 6.8.

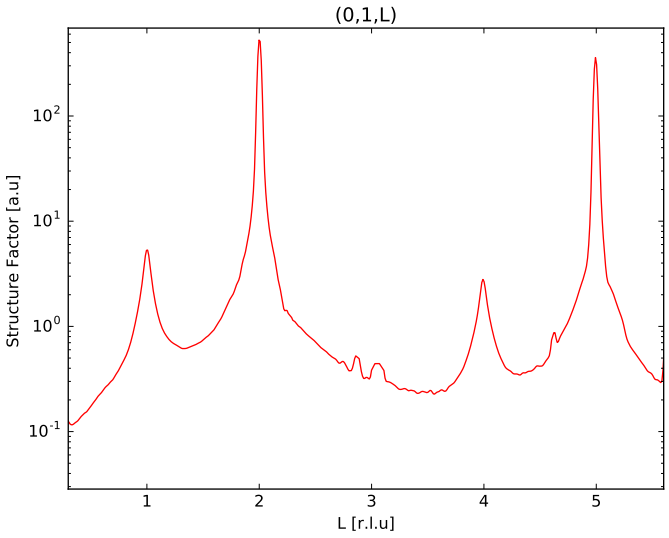

Figure 6.10: Integrated CTR along $(h, k, l) = (0, 1, L)$. We have two new peak at position L equal to 1 and 4.

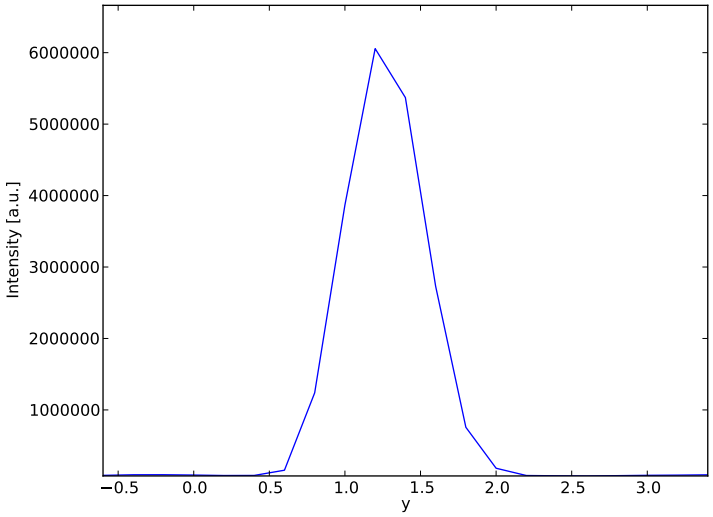

Figure 6.11: Scan of the intensity moving the sample in the y direction. The detector was fixed in the corresponding position of $(h, k, l) = (0, 1, 1)$ in the reciprocal space. The other coordinates of the sample were:$(x, y, z) = (-0.001, y, 0.0487)$.

on the Ag(111) surface. Therefore, the planes stacked without following the 'correct' sequence, instead of ABCABC stacking, we have ABCBCA. In fact, in Fig. 6.10 we can see that the periodicity of the peaks is always the same $\Delta L = 3$, but the position of these new peaks is shifthed by one, in comparison to what should be their correct position. These peaks appearing at 'wrong' Bragg position are called *stacking faults*.
In order to understand where we formed the stacking faults and their dimension, the detector was fixed in the characteristic position of the stacking fault peak $(h, k, l) = (0, 1, 1)$. Then, the sample was moved in the y direction and the intensity of the peak was recorded. As shown in the Fig. 6.11, the intensity has a maximum near the value of $y = 1.4$. When the sample is moved in the y direction, the intensity goes to zero. The position for which the intensity is maximum, corresponds to the sample position during the previous oxidation recorded in the timescan 6.8. This means that we had a region of bulk oxide on the sample surface only where we enlightened with the beam. The formation of island of bulk oxide was already observed in a past study [23], the new could be that the island are beam induced. The hypothesis of the process is that the beam induces the formation of bulk oxide and after the increasing of the temperature, the oxygen starts to desorb from it and then stacking faults are formed.
Finally, the temperature was increased to remove the stacking faults. In particular two cycles of annealing at very high temperature were done (up to $930K$). At the end, the peak in position $(h, k, l) = (0, 1, 1)$ disappeared.

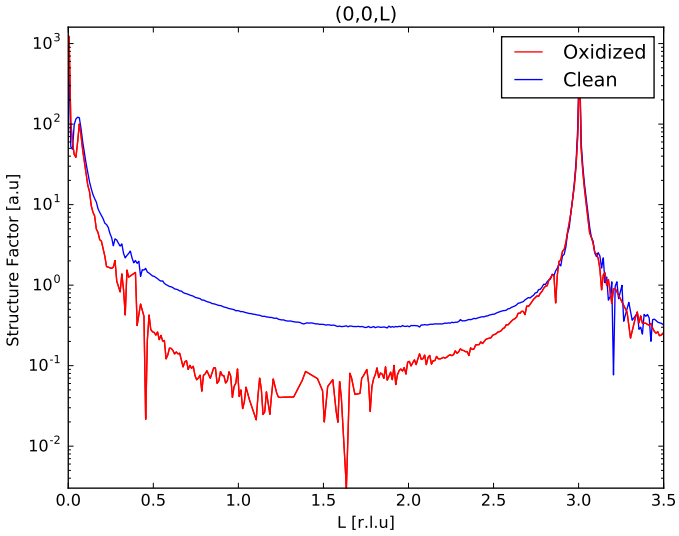

Figure 6.12: Comparison between the XRR carried out, at the beginning of the experiment, from the clean surface and the XRR after the oxidation process.

6.3.2 Restoring of a clean Ag (111) surface

The fig.6.12 shows two X-Ray Reflectivity curves. The blue one is the XRR curve of the clean surface, shown previously. The red one was acquired after the oxidation of the surface. The oxidation leads to the formation of reconstructions on the surface, so the roughness of the surface is increased. This is perfectly demonstrated by the XRR measure, where is present an important decreasing of intensity between the Bragg's peaks. In order to restore the clean surface and continue with the experiment, many cycles of annealing were done. In particular, the sample was heated for 15 minutes for every cycles and up to 923K. The result of this cleaning procedure is shown in Fig. 6.13. The two curves in this case are very similar, it means that the surface became again smooth.

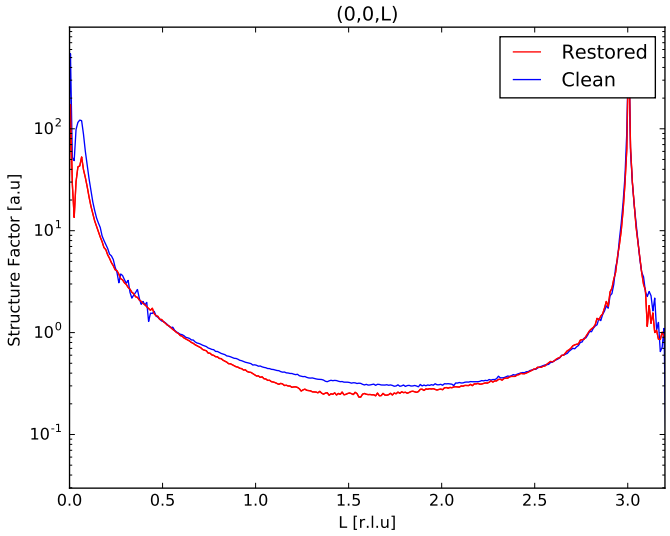

Figure 6.13: Comparison between the XRR of the clean surface and the XRR of the oxidized surface after cycles of sputtering and annealing.

6.3.3 Stability of the Bulk Oxide

After the restoring of the initial conditions of cleanliness and smoothness, the Ag(111) surface was oxidized again. Environmental conditions, temperature and radiation dose, were changed with the aim to investigate the bulk oxide stability. The first measurement represents a timescan acquired at the $(h, k, l) = (0, 0.86, 0.87)$ position. The sample was not heated, the pressure was 0.4 mbar of Oxygen and the radiation dose was at its maximum (attenuator set to 0). The intensity, as shown in Fig.6.14, grows linearly with the time, we can say that at this conditions, the growth rate of the bulk oxide follows this trend. On the contrary, in Fig.6.15, is shown a very unstable peak. The condition in this case were, oxygen presure of 0.32 mbar, temperature at 323K and attenuator set to 0. What can be observed in this timescan is a delay between the oxide formation and the presence of oxygen inside the chamber. This particularity, was observed for several timescan. The peak starts always to increase significantly after a while. That could mean, that only the presence of oxygen is not enough for the formation of bulk oxide, but also the beam is necessary. This could be considered another proof that the beam induces the formation of bulk oxide on the Ag (111) surface.

As the hypothesis is that the beam could induce the formation of bulk oxide, we acquired three timescans in the bulk oxide position, each one with a different attenuator factor. The higher is the attenuator factor, the lower is the intesity of the beam that reaches the sample. The measures are shown in Fig. 6.16, in particular, the slope of the curve is reduced with the increase of the attenuator factor. This could be considered another evidence that the beam influences the formation of Bulk oxide over Ag (111) surface.

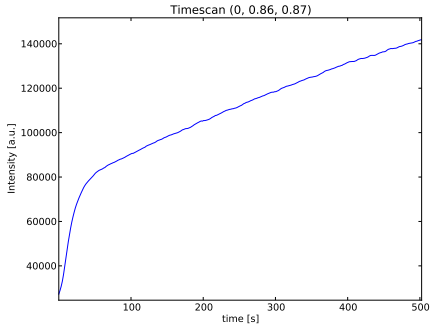

Figure 6.14: Timescan in the position $(h, k, l) = (0, 0.86, 0.87)$. Bulk oxide formed with a linear slope at room temperature and at 0.4 mbar of Oxygen. The attenuator was set to 0.

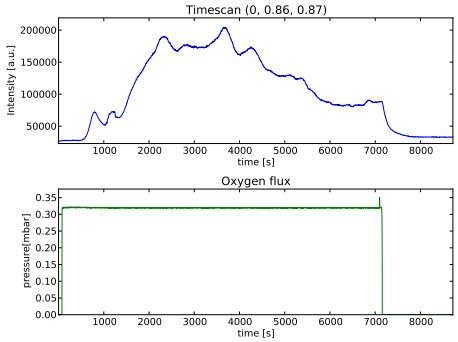

Figure 6.15: In the top of the image: Timescan in the position $(h, k, l) = (0, 0.86, 0.87)$. Bottom: Flow of the oxygen. Temperature: 323K. Unstable structure.

6.4 Flow Ethylene inside the flow reactor

In the last part of the experiment the ethylene was flowed inside the flow reactor. In particular, ethylene and oxygen were both flowed with the aim to obtain the reaction catalysed by silver surface. Different pressures of the reactants were tested. Before flowing ethylene inside the reactor, the surface was oxidized again. The presence of the bulk oxyde peak at $(h, k, l) = (0, 0.87, 0.86)$, was confirmed by measurements. Therefore, we made a timescan in this position. The measure is shown in fig. 6.17, where the timescan, the flow of oxygen and ethylene are displayed. Their initial pressures were 0.5 mbar for oxygen and 0.007 mbar for ethylene. Their pressures were changed in time. In particular, at the beginning of the measurement, the pressure of ethylene was increased up to 0.003 mbar and the intensity of the peak of bulk oxide decreased rapidly.

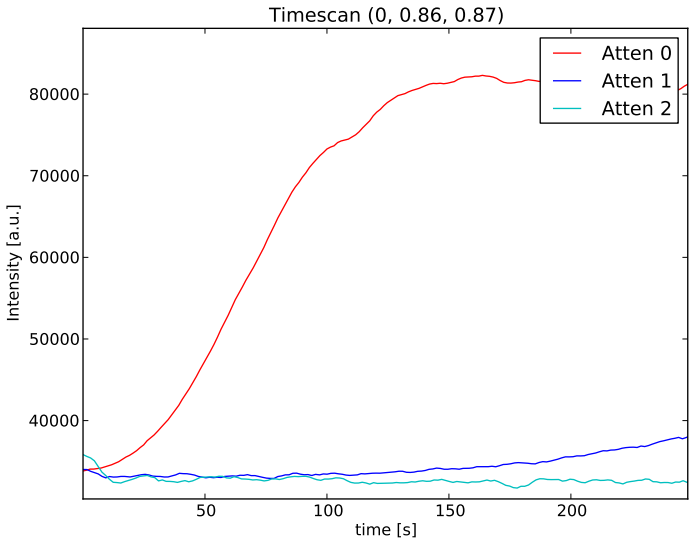

Figure 6.16: Timescans in the same position: $(h, k, l) = (0, 0.86, 0.87)$. Each curves has a different attenuator factor.

On the contrary, when its pressure was set again to the initial value, the peak started to increase. We had the formation of bulk oxide, because, as shown in the previous paragraph, the conditions were suited for its growth (0.05 mbar of Oxygen and room temperature). Finally, when the pressure of ethylene was set to 0.05 mbar the newly formed peak disappeared (the intensity decreases of the 87% of its maximum value), more rapidly than before. Moreover, the peak disappeared despite the pressure of Oxygen was increased in steps during the time. At the end of this measure the temperature was increased at 373 K. Subsequently, we moved the detector in different positions for checking the presence of other reconstruction on the surface. In the typical positions of the $p(4 \times 4)$ no peaks were found. So, after the flowing of ethylene neither $p(4 \times 4)$ reconstruction nor bulk oxide were present. What was found, were again stacking faults, but also in this case they were due to the heating of the sample. As discussed in the previous paragraph, the increasing of temperature leads to the stacking faults formation. So, we decided to put the detector in their characteristic position $(h, k, l) = (0, 1, 1)$ and recorded a timescan while the pressure of oxygen and ethylene were changed. The timescan and the fluxes are shown in fig. 6.18. The decreasing trend of the curve is due to the increase of the temperature before the measure, until 873 K. The pressure settings at the beginning of the timescan were 0 mbar of Oxygen and 0.002 mbar of Ethylene. The oxygen pressure was increased during the timescan, until 0.5 mbar, but this didn't influence the intensity. On the contrary, when the pressure of Ethylene was set to 0.35 mbar, the intensity dropped down rapidly. In conclusion, what emerged from these measures is that the presence of ethylene removes all of the reconstructions that we have studied. p(4×4) is not present after the flowing of ethylene in the reactor,

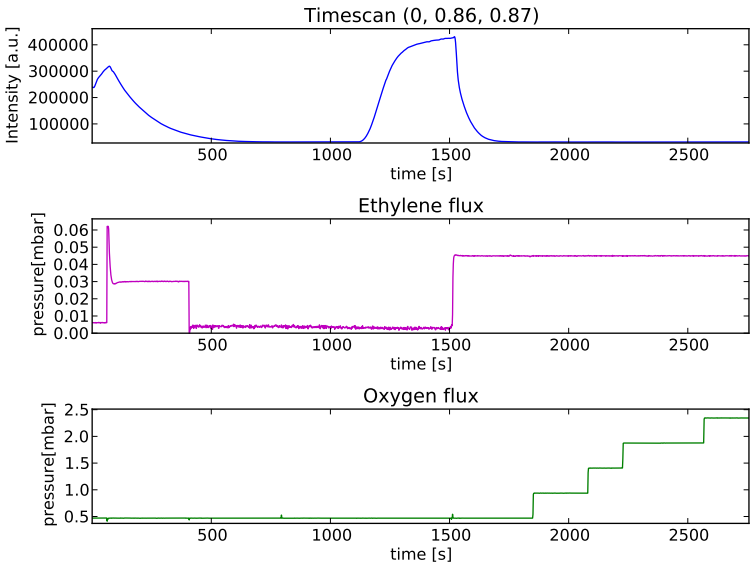

Figure 6.17: In the top part: Timescan in position $(h, k, l) = (0, 0.86, 0.87)$. In the middle: Pressure of Ethylene inside the Flow reactor changing in time. In the bottom part: Oxygen pressure as function of time.

whereas for bulk oxide and stacking faults we measured their disappearance. What can be hypothesized, is the happening of the combustion reaction between ethylene and oxygen, that as discussed in the introduction is more favoured in these conditions and this exothermic process etched all the reconstructions present on the surface.

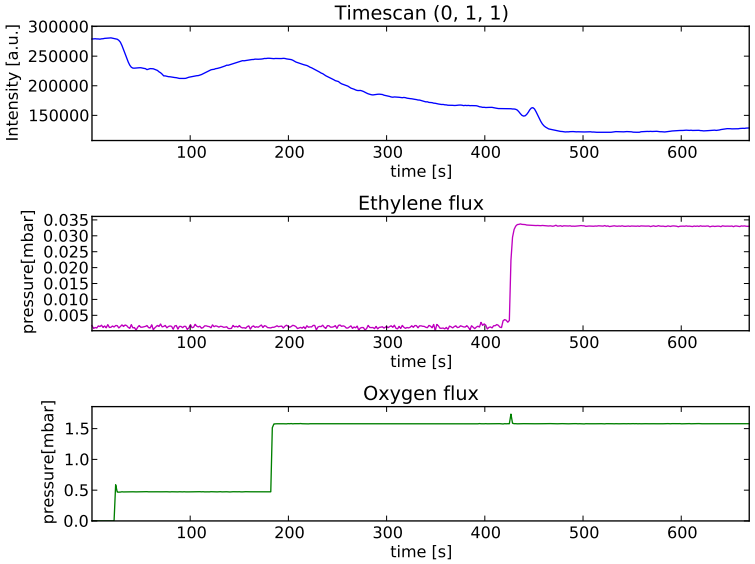

Figure 6.18: Timescan in the position $(h, k, l) = (0, 1, 1)$. Below are shown the flux of Ethylene and Oxygen.

Chapter 7

Conclusions

This in-situ SXRD study of the oxidation of Ag(111) surface, was aimed to find the oxygen-induced structure which is the active phase for the catalytic reaction, ethylene epoxidation. The use of this experimental technique for this topic is almost pioneristic, because it was carried out only one time before by Schmid et.al.[31]. The results of our experiment nearly match with the ones of the previous study. In particular in our investigation we observed two of the three structures candidate to be the catalytic active phase: the well known p-(4×4) reconstructure and the bulk oxide. During the experiment we verified the formation of the p-(4×4) but also its instability by increasing the oxygen pressure and finally its disappearing. The structure that was formed after this increasing was not a surface oxide but a thick bulk oxide. We observed too the growth of the bulk oxide in the Stranski–Krastanov-like growth, but we demonstrated its instability at a temperature higher than 373K. Moreover, we observed, after a further increase of the temperature, the desorption of oxygen atoms from the bulk oxide and the conseguently creation of stacking faults, which arise from the uncorrect stacking of the Ag planes. This was a further proof of the inverted growth of the bulk oxide on Ag(111) surface. We observed too, the formation of islands of bulk oxide instead of a full coverage of the surface, but we undestood that these islands are formed on the surface only where the beam enlights. Moreover, we observed that the growth rate of the bulk oxide strongly depends on the radiation dose, in particular it forms more rapidly when the dose is at maximum. The presence of the beam seems to be essential, infact there is always a delay between the oxygen exposure and the growth of the bulk oxide. In addition, even if the sample is kept at high temperature and oxygen pressure for some time without the beam, we observed a significant increasing of the oxide signal only after the exposure of the sample to the beam. In the last part of the experiment we tried to simulate the reaction conditions by flowing a mixture of oxygen and ethylene inside the flow reactor, but it was a failure, we only verified that all the reconstructions formed on the surface after the oxidation disappeared. Finally, our hypothesis is that the synchrotron radiation induces the oxidation of the Ag(111) surface and, for this reason, the SXRD is not the suitable tool for this research.

Bibliography

[1] Neil W Ashcroft. *ND Mermin Solid state physics*. 1976, p. 120.

[2] O Balmes et al. "The ID03 surface diffraction beamline for in-situ and real-time X-ray investigations of catalytic reactions at surfaces". In: *Catalysis Today* 145.3 (2009), pp. 220–226.

[3] Lamberto Duò-Alberto Brambilla. *Interazione Radiazione-Materia*. Tech. rep. Politecnico di Milano, 2013.

[4] Charles T. Campbell. "Atomic and molecular oxygen adsorption on Ag(111)". In: *Surface Science* 157.1 (1985), pp. 43–60. ISSN: 0039-6028. URL: http://www.sciencedirect.com/science/article/pii/003960288590634X.

[5] Charles T. Campbell. "Chlorine promoters in selective ethylene epoxidation over Ag(111): A comparison with Ag(110)". In: *Journal of Catalysis* 99.1 (1986), pp. 28–38. ISSN: 0021-9517. URL: http://www.sciencedirect.com/science/article/pii/0021951786901958.

[6] CI Carlisle et al. "Imaging the surface and the interface atoms of an oxide film on Ag {111} by scanning tunneling microscopy: Experiment and theory". In: *Physical review letters* 84.17 (2000), p. 3899.

[7] Sharon S Chadwick. "Ullmann's Encyclopedia of Industrial Chemistry". In: *Reference Services Review* 16.4 (1988), pp. 31–34.

[8] Kenton D Childs et al. "Handbook of Auger electron spectroscopy". In: *Physical Electronics,* (1995).

[9] Jonathan Derouin et al. "Formation of surface oxides and Ag2O thin films with atomic oxygen on Ag(111)". In: *Surface Science* 641 (Nov. 2015), pp. L1–L4. ISSN: 0039-6028. URL: http://www.sciencedirect.com/science/article/pii/S0039602815001958.

[10] Robert B Grant and Richard M Lambert. "Mechanism of the silver-catalysed heterogeneous epoxidation of ethylene". In: *Journal of the Chemical Society, Chemical Communications* 12 (1983), pp. 662–663.

[11] André Guinier. *X-ray diffraction in crystals, imperfect crystals, and amorphous bodies*. Courier Corporation, 1994.

[12] BLM Hendriksen and JWM Frenken. "CO oxidation on Pt (110): scanning tunneling microscopy inside a high-pressure flow reactor". In: *Physical Review Letters* 89.4 (2002), p. 046101.

[13] *http://medipix.web.cern.ch/medipix/pages/medipix1.php.*
[14] *https://en.wikipedia.org/wiki/Bragg_plane.*
[15] *https://goo.gl/Ja06O1.*
[16] Suljo Linic and Mark A Barteau. "Control of ethylene epoxidation selectivity by surface oxametallacycles". In: *Journal of the American Chemical Society* 125.14 (2003), pp. 4034–4035.
[17] Hans Luth. *Solid surfaces, interfaces and thin films*. Vol. 4. Springer, 2001.
[18] RG Musket et al. "Preparation of atomically clean surfaces of selected elements: a review". In: *Applications of Surface Science* 10.2 (1982), pp. 143–207.
[19] *Operating and Maintenance Handbook Millennia Series 2-IGC2 Ionisation Gauge Controller.*
[20] Kenjiro Oura et al. *Surface science*. Springer, 2003.
[21] Kenjiro Oura et al. *Surface science: an introduction*. Springer Science & Business Media, 2013.
[22] H Over et al. "Atomic-scale structure and catalytic reactivity of the RuO2 (110) surface". In: *Science* 287.5457 (2000), pp. 1474–1476.
[23] A Reicho et al. "Stranski–Krastanov like oxide growth on Ag (111) at atmospheric oxygen pressures". In: *Surface science* 601.4 (2007), pp. L19–L23.
[24] Alexander Reicho. "Ambient pressure oxidation of Ag (111) surfaces: an in-situ X-ray study". PhD thesis. 2008.
[25] I K Robinson and D J Tweet. "Surface X-ray diffraction". In: *Reports on Progress in Physics* 55.5 (1992), p. 599. URL: http://stacks.iop.org/0034-4885/55/i=5/a=002.
[26] IK Robinson. "Crystal truncation rods and surface roughness". In: *Physical Review B* 33.6 (1986), p. 3830.
[27] IK Robinson and DJ Tweet. "Surface x-ray diffraction". In: *Reports on Progress in Physics* 55.5 (1992), p. 599.
[28] Sander Roobol et al. "BINoculars: data reduction and analysis software for two-dimensional detectors in surface X-ray diffraction". In: *Journal of applied crystallography* 48.4 (2015), pp. 1324–1329.
[29] G. Rovida et al. "Chemisorption of oxygen on the silver (111) surface". In: *Surf. Sci.* 43.1 (May 1974), pp. 230–256. ISSN: 0039-6028. URL: http://www.sciencedirect.com/science/article/pii/0039602874902295.
[30] Charles N Satterfield. "Heterogeneous catalysis in industrial practice". In: (1991).
[31] Michael Schmid et al. "Structure of Ag (111)- p (4× 4)- O: No Silver Oxide". In: *Phys Rev Lett* 96.14 (2006), p. 146102.
[32] Oliver H Seeck and Bridget Murphy. *X-ray Diffraction: Modern Experimental Techniques*. CRC Press, 2015.
[33] R Van Rijn et al. "Ultrahigh vacuum/high-pressure flow reactor for surface x-ray diffraction and grazing incidence small angle x-ray scattering studies close to conditions for industrial catalysis". In: *Review of Scientific Instruments* 81.1 (2010), p. 014101.

[34] Klaus Wandelt. *Surface and Interface Science, Volumes 1 and 2: Volume 1-Concepts and Methods; Volume 2-Properties of Elemental Surfaces*. Vol. 1. John Wiley & Sons, 2012.

[35] Philip Willmott. *An introduction to synchrotron radiation: techniques and applications*. John Wiley & Sons, 2011.